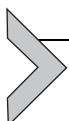


State observation and feedback control in robotic systems for therapy and surgery

Bita Fallahi, Lingbo Cheng and Mahdi Tavakoli

Department of Electrical and Computer Engineering, University of Alberta, Edmonton, AB, Canada

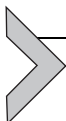


1 Introduction

Steerable needles are used in different minimally invasive procedures such as brachytherapy, biopsy, and neurosurgery. In these methods, hollow long flexible bevel-tipped needles are inserted into the human body for diagnosis, treatment, or sample removal. During these procedures, the targeted organs and the needles are monitored using different imaging methods such as ultrasound (US), fluoroscopy, and X-ray. Accurate needle positioning minimizes the undesirable side effects on the healthy and neighboring tissue and is a crucial factor in determining the efficiency of these methods. The desired needle path depends on the application. In biopsy, it is desired to reach a constant final deflection, whereas in brachytherapy the needle should follow a straight path. In case of having obstacles on the needle path (such as bones or nerves), the needle should follow a preplanned curved. In general, needle deflection, tissue deformation, and limitations in controlling the needle from outside the body are the challenges in accurate needle tip positioning, which are discussed in [Section 2](#).

[Section 3](#) is devoted to robot-assisted surgical systems for beating-heart surgery. Cardiovascular disease is one of the leading causes of death worldwide. Conventional extra-and intracardiac surgeries need the heart to be arrested by connecting the patient to a cardiopulmonary bypass (CPB) machine ([Ruszowski et al., 2015](#)). However, arrested-heart surgery has adverse effects due to using CPB ([Dacey et al., 2005; Newman et al., 2001; Paparella et al., 2002; Zeitlhofer et al., 1993; Bellinger et al., 1999](#)). Different from arrested-heart surgery, beating-heart surgery could eliminate such negative effects of CPB by allowing the heart to beat normally ([Angelini et al., 2002](#)), and could also enable intraoperative evaluation of the heart tissue

motion, which is critical to the assessment of reconstructive heart operations such as mitral valve surgery (Fix et al., 1993). The most prominent challenge to be addressed for beating-heart surgery is the rapid motions of the heart whose movement velocity and acceleration are approximately 210 mm/s and 3800 mm/s², respectively (Kettler et al., 2007). Manual tool position compensation according to the heart motion will not only lead to the human operator's fatigue and exhaustion but risks tool-tissue collision and tissue injury. The application of robot-assisted surgical systems and control methods for synchronizing the surgical robot's motion with the beating heart's motion are discussed in Section 3.



2 Needle insertion procedures

Prostate cancer is the second frequent cancer in men around the world, with an estimation of 1.1 million new cases to have occurred in 2012 (Torre et al., 2015). One leading treatment option for early-stage prostate cancer is US-guided brachytherapy, which is a type of radiotherapy. In this method, radioactive seeds are implanted around the prostate gland to deliver the radiations internally. The margins of the prostate and the target volume are found using preoperative axial images and are further used for preplanning the seed locations and the dosage distribution. The seed implantation is accompanied by intraoperative transrectal ultrasound (TRUS) images to provide visual information for needle guidance. These images, as well as the desired seed locations, are registered with respect to a 5-mm grid template. Several needles loaded with radioactive seeds are inserted through the template, and it is desired to insert the needle on a straight path to the final depth. The seeds are implanted on the needle track by retracting the needles and pushing out the seeds using a stylet. In brachytherapy, the preplanned location of the seeds is a determinant factor in defining radiation dosage and therefore is of great importance. Errors in the seed positioning reduce the method efficiency as instead of cancerous tissue, healthy tissue is imposed to the radiations.

Using a grid template, the desired path to the final depth is a straight line. However, this can only be true if there are no sensitive tissue such as nerves, blood vessels, or bones are on the needle path. In the case of pubic arch interference, which is common in patients with large prostate (Wallner et al., 1999), the needle path to the anterior prostate is obstructed. In such case, the needle should be steered on a desired curved path to go around the obstacle and reach the final depth. This scenario is in demand of finding feasible and

collision-free trajectories from the insertion point to the final point and steering the needle on the desired path. Steering the needle on the desired path can be done using axial needle rotations to change the bevel orientation, insertion velocity, needle base lateral position, and needle base force/torque.

In manual insertions performed by experienced practitioners, the absolute seed positioning error is about ± 5 mm (Taschereau et al., 2000). To improve the seed positioning, intelligent assistant robots can be used to steer the needle toward the target and compensate for the errors caused by the needle and tissue deformation. In robot-assisted procedures, for safety reasons, it is desired to split the tasks between the clinician and the robotic system to keep the clinician in the loop. For example, the robotic system only controls the needle rotations, whereas the surgeon selects the initial insertion point and performs the insertion.

2.1 Related work

Depending on the application, different scenarios are possible in needle insertion procedures. For all situations, the first step is to plan the desired trajectory. The path planner should consider the insertion and target points, the location of the obstacles, and the constraints on the needle motion. Similar to path planners, motion planners provide not only a feasible path but also the control inputs required for following the path (Minhas et al., 2007; Schulman et al., 2014; Wang et al., 2014; Moreira et al., 2014a; Majewicz et al., 2014). However, in order to compensate for the errors caused by tissue nonhomogeneity and modeling uncertainties, replanning is necessary, which requires the motion planners to be computationally fast (Duan et al., 2014).

Another way to deal with the steering problems is to use feedback control strategies (Abolhassani et al., 2007; Haddadi et al., 2010; Abayazid et al., 2013; Rucker et al., 2013; Khadem et al., 2016; Sovizi et al., 2016; Fallahi et al., 2016b, 2017, 2018). This approach is based on the closed-loop feedback structure to calculate the control inputs. In motion planning, the steering commands are calculated for the current and future times, however, in feedback control methods, the commands are found only for the present time. By taking the desired path (found by any path planner), the controller is responsible for calculating the control commands to compensate the errors. The planner/controller should be provided with information about needle forces, needle shape, and tip pose (position and/or orientation) in real time. However, due to the nature of the procedures, in many situations,

some of these variables cannot be measured directly. As the needle is inserted into the tissue, the needle is tracked using imaging modalities. The images are combined with image processing techniques to translate visual information into numerical values to be used by the computers. US imaging is a cost effective and widely used imaging modality, which can be used to track the needle and find the needle tip position. There have been different methods proposed in the literature for image registration and needle position and shape estimation using US images ([Uhercik et al., 2009](#); [Asadian et al., 2011](#); [Zhao et al., 2012, 2013](#); [Malekian et al., 2013](#); [Kaya and Bebek, 2014](#); [Waine et al., 2016](#); [Rossa et al., 2016](#)).

However, using the US images, it is not possible to measure the needle tip orientation as the low-resolution images, and the small diameter of the needle does not provide sufficient information for detecting the needle tip heading. Moreover, due to the limitations on the sensor dimensions and the sterilization issues, using needle-mounted pose or force sensors in clinical applications is not practical. This limitation is the motivation to employ observation methods and estimate the nonmeasurable variables using the mathematical models and the measured variables. In the sequel, we first provide an overview of needle steering modeling and then focus on different methodologies proposed for state observation, planning, and control in needle steering.

2.2 Modeling

The design and programming of needle steering systems require a suitable model that represents the system's behavior and describes the relation between the system inputs and outputs. There have been different modeling approaches proposed in the literature such as finite element methods ([DiMaio and Salcudean, 2003, 2005](#); [Goksel et al., 2006](#); [Dehghan and Salcudean, 2009](#)), flexible beam theory ([Yan et al., 2006, 2009](#); [Chentanez et al., 2009](#)), energy-based methods ([Misra et al., 2010](#)), and the kinematic model ([Webster et al., 2006](#)). The kinematic model proposed by [Webster et al. \(2006\)](#) is a nonholonomic model. In this model, the needle is assumed to move on a curved path with constant curvature (circle). As the needle path curvature depends on the needle and tissue properties, for each needle/tissue combination, the needle path curvature should be found using curve-fitting methods. The main advantage of this model is its simplicity. It provides an intuitive and computationally efficient method for predicting needle deflection, which makes it suitable for planning and control purposes.

In this model, the motion of the needle resembles the motion of a unicycle and its kinematics are found as [Webster et al. \(2006\)](#)

$$\dot{g}_{ab}(t) = g_{ab}(t)(v \hat{V}_1 + u \hat{V}_2) \quad (1)$$

with

$$V_1 = \begin{bmatrix} e_3 \\ \kappa e_1 \end{bmatrix}, \quad V_2 = \begin{bmatrix} 0_{3 \times 1} \\ e_3 \end{bmatrix} \quad (2)$$

where the operator $(\hat{\cdot})$ is defined as

$$\hat{\cdot} : \begin{bmatrix} \omega_1 \\ \omega_2 \\ \omega_3 \end{bmatrix} \mapsto \begin{bmatrix} 0 & -\omega_3 & \omega_2 \\ \omega_3 & 0 & -\omega_1 \\ -\omega_2 & \omega_1 & 0 \end{bmatrix} \quad (3)$$

In Eq. (1), $g_{ab} = \begin{bmatrix} R_{ab} & P_{ab} \\ 0^T & 1 \end{bmatrix}$ is the rigid transformation between frames $\{A\}$ and $\{B\}$, as shown in [Fig. 1](#). The vector $P_{ab} = [x \ y \ z]^T$ and the matrix R_{ab} represent the position and the orientation of the moving frame $\{B\}$ with respect to the fixed frame $\{A\}$, respectively. v and u are the insertion velocity and the needle axial rotational velocity, respectively, and $e_i (i = 1, 2, 3)$ represent the standard basis vectors in \mathbb{R}^3 . κ is the needle path curvature, which due to the tissue nonhomogeneity encounters uncertainty. This value, however, is considered to be bounded, and its bounds can be determined preoperatively and be written as $\underline{\kappa} < \kappa < \bar{\kappa}$.

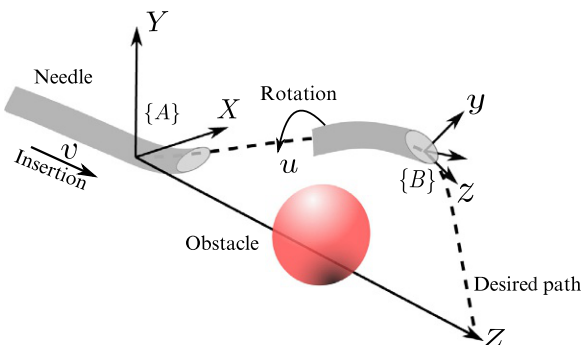


Fig. 1 The needle in 3D space, desired path and obstacle. Frame $\{A\}$ is the fixed frame and frame $\{B\}$ attached to the needle tip is the moving frame. v and u are the insertion and rotation velocity, respectively.

The coordinates free representation (1) can be expanded to

$$\dot{p} = R \begin{bmatrix} 0 \\ 0 \\ v \end{bmatrix} \quad (4a)$$

$$\dot{R} = R \begin{bmatrix} 0 & -u & 0 \\ u & 0 & -\kappa v \\ 0 & \kappa v & 0 \end{bmatrix} \quad (4b)$$

Defining the vector $\mathbf{q} = [x, \gamma, z, \alpha, \beta, \gamma]^T$ as the generalized coordinates, which is well defined on

$$\mathcal{U} = \{\mathbf{q} \in \mathbb{R}^6 : \alpha, \gamma \in \mathbb{R}, \beta \in [-\pi/2, \pi/2]\} \quad (5)$$

Kallem and Cowan (2009) have presented the Z - Y - X representation of the needle kinematics (1) as

$$\dot{x} = v \sin \beta \quad (6a)$$

$$\dot{y} = -v \cos \beta \sin \alpha \quad (6b)$$

$$\dot{z} = v \cos \alpha \cos \beta \quad (6c)$$

$$\dot{\alpha} = \kappa v \cos \gamma \sec \beta \quad (6d)$$

$$\dot{\beta} = \kappa v \sin \gamma \quad (6e)$$

$$\dot{\gamma} = -\kappa v \cos \gamma \tan \beta + u \quad (6f)$$

The values α , β , and γ are the yaw, pitch, and roll angles, respectively, and represent the orientation of the origin of the moving frame $\{B\}$ with respect to the fixed frame $\{A\}$. The relation between the rotation matrix R and the three angles is given by premultiplying the three basic rotations about the axes of the fixed frames (Taghirad, 2013). In reality, due to the presence of the tissue and the limited curvature of the needles, the angles α and β remain bounded, and more bending is related to larger values of these angles. The upper bound on these angles, which depend on the desired path traveled by the needle, can be determined in the planning level. Therefore, it is assumed that $|\alpha| < \alpha^*$ and $|\beta| < \beta^*$ with $\alpha^*, \beta^* \in [0, \pi/2]$.

In Eq. (6), by setting $\beta = 0$ degrees and $\gamma = 0, 180$ degrees, the two-dimensional (2D) needle motion can be found as

$$\begin{bmatrix} \dot{Z} \\ \dot{y} \\ \dot{\alpha} \end{bmatrix} = \begin{bmatrix} \cos\alpha \\ \sin\alpha \\ \pm\kappa \end{bmatrix} v \quad (7)$$

The earlier equation represents the planar deflection of the needle in Y-Z plane. In this case, the \pm sign determines the two possibilities for the bevel orientation as well as the concavity of the needle path curve in the plane as shown in Fig. 2. This model is later extended to account for paths with variable curvature by using an omnidirectional wheel (Fallahi et al., 2015).

2.3 Measurement and observation

In manual needle insertion procedures, the surgeon tracks the needle visually using imaging modalities. US imaging is a fast, widely used, and cost-effective method, which compared to other modalities such as magnetic resonance imaging and computed tomography, provides real-time tracking of the needle during the procedure. This visual information can be translated into numerical values using image processing techniques and be used in feedback computations. Different methods have been proposed in the literature for needle localization, that is, estimating the needle position in US images. Rossa et al. (2016) proposed a method for predicting the needle tip position using the deflection of a single point along the needle. Random sample consensus (RANSAC) is a robust method to fit polynomials on the curves in the three-dimensional (3D) space (Uherčík et al., 2009). This iterative method employs a set of observed data and deals with outliers to find the model parameters. Combining this method with Kalman filters reduces the search area and speeds up the algorithm (Zhao et al., 2012, 2013). Waine

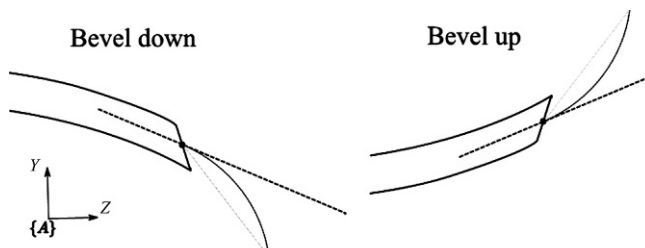


Fig. 2 Two possible orientations of the bevel in planar motion.

[et al. \(2016\)](#) have employed the RANSAC algorithm to find the needle tip position using 2D US images. [Malekian et al. \(2013\)](#) combine the RANSAC algorithm with a denoising method to increase the accuracy. [Asadian et al. \(2011\)](#) estimated the needle tip velocity from a noisy position using a high-gain observer.

In these methods, the needle tip position is acquired from the US images and the word “estimation” is used. However, since using needle-mounted sensors is not clinically feasible, the US images are the only source of position measurements, and therefore, the estimated values should be accepted as the true position “measurement.”

Besides, according to Eq. (6), acquiring information about the needle tip heading is advantageous in controlling the needle tip position. However, it is not possible to measure the orientation parameters using US images, since due to the small diameter of the needle and the low resolution of the images, the bevel orientation is not detectable. Measuring the orientation requires utilizing sensors such as needle-mounted electromagnetic tracking sensor, which suffers from sterilization issues. The controller designed in [Rucker et al. \(2013\)](#) requires all the orientation parameters. This controller is implemented using a five-DOF magnetic tracking sensor and combined with a Kalman filter. However, since suitable sensors are not accessible, state observers can be employed to estimate the needle tip orientation. The state observers are computer-implemented systems, which run concurrently to the real system. The observer equations are formed using the system equations and additional corrective terms. If the observer is convergent, its states provide an estimate of the system’s nonmeasurable state. [Kalle and Cowan \(2009\)](#) use the 3D kinematic equations (6) and design a linear observer/controller. Later, this observer is used in many other works. [Reed et al. \(2008\)](#) employed the linear observer to estimate the needle tip orientation and used the estimated variables in a low-level controller, which works along with a high-level 2D planner to steer the needle on the optimal path. In [Motaharifar et al. \(2015\)](#), the same transformation is used, and a nonlinear observer is designed to be used with an adaptive controller. In [Kalle et al. \(2011\)](#), this linear observer is designed for the reduced configuration space and is fed to the fiber space observer to estimate the full system states for a planar task. In [Swensen et al. \(2014\)](#), a model for torsional dynamics of the needle is presented and augmented with planar variables. The system is then linearized, and a Kalman filter is employed to estimate the system states and apply a state feedback control. Using Eq. (6) and the nonlinear

transformation $s = [x \ v\sin\beta \ -\kappa\nu^2\cos\beta\sin\gamma]^T$, the system equations can be written as

$$\dot{s} = As + B\phi \quad (8a)$$

$$\gamma = Cs \quad (8b)$$

with

$$A = \begin{bmatrix} 0 & 1 & 0 \\ 0 & 0 & 1 \\ 0 & 0 & 0 \end{bmatrix}, \quad B = \begin{bmatrix} 0 \\ 0 \\ 1 \end{bmatrix}, \quad C = [1 \quad 0 \quad 0], \quad \phi = \nu' \quad (9a)$$

where $\nu' = \kappa^2\sin\beta - \kappa\nu^2(\cos\beta\cos\gamma)u$ is defined as the new control variable and the observer is formulated as $\dot{\hat{s}} = A\hat{s} + B\phi + L(\gamma - \hat{\gamma})$. In this equation, (\cdot) denotes the estimated values and L is the observer gain to be designed such that $A + LC$ is Hurwitz. Using the linear observer, an observer-based linear controller is designed in [Kalle and Cowan \(2009\)](#), which due to the singularities in the nonlinear system, can only be applied to stabilize the needle in one plane. In [Fallahi et al. \(2016a\)](#), the same transformation is used, however, instead of linearizing the whole system, the term ϕ is selected as

$$\phi = -(\kappa\nu)^2 s_2 \pm \kappa\nu^2 u \sqrt{1 - (s_2^2 + s_3^2)} \quad (10)$$

and its effect is considered by rewriting the observer equations as $\dot{\hat{s}} = A\hat{s} + \hat{\phi} + \Delta_\theta L(\hat{\gamma} - \gamma)$ with $\Delta_\theta = \text{diag}\{\theta, \theta^2, \theta^3\}$ and $\theta > 1$. The problem with the nonlinear observer in this form is that ϕ does not satisfy the Lipschitz continuity condition, and the convergence of the observer is guaranteed for certain assumptions to keep the states bounded. Due to the small number of researches performed for estimating the needle tip orientation, this subject remains open for further studies.

2.4 Planning

The nonholonomic constraints on the needle kinematics confine the needle moves to a set of reachable points and limit the trajectories that can be followed by the needle. Considering the location of the obstacles and the constraints on the needle, the path planner is responsible for finding a feasible, collision-free path from the insertion point to the target. Depending on the planning method used, other criteria such as parameter uncertainty, noise, and optimizations can be taken into account. A motion planner,

however, not only plans the desired trajectory but also finds a sequence of commands for steering the needle on the planned trajectory. In other words, motion planning is a combination of path planning and an implementation method. In the ideal situation, these commands should steer the needle on the desired trajectory. However, in reality, due to the modeling and parametric uncertainties, noise, and tissue nonhomogeneity, the needle position deviates from the desired trajectory. In Schulman et al. (2014), the errors are compensated by insertion, partial retraction, rotation, and further insertion of the needle. However, retractions and reinsertions are not desirable as they increase the tissue trauma. Another solution for dealing with uncertainties is to perform replanning to compensate for the errors caused by tissue nonhomogeneity. Wang et al. (2014) propose the planner for dynamic environments using a mass-spring model for the deformable tissue. The dynamic planner is equipped with a vision system to track the radius of curvature, which is used in replanning and updating the path to adapt to the changes in the position and curvature. Such performance, however, requires the planner to be fast enough. Duan et al. (2014) show by experiments that the computations are done in 1.6 s which enables replanning for error compensation.

The desired path can be either a constant-curvature path or a variable-curvature path. A constant-curvature path is composed of a sequence of circular segments. Considering the axial needle rotations as the main control input, proper changes in the needle tip orientation at each segment steers the needle on the desired path. This can be done by the stop-turn strategy. In this strategy, the insertion and rotation commands are separated, meaning that for each segment, the needle is purely inserted to a certain depth and is stopped to perform the rotation, and the rotated frame is propagated by further insertion (Duindam et al., 2008). In this case, the output of the motion planner is the depth and the magnitude of rotation.

A variable-curvature path is a curved path with different curvatures along it. The strategy for steering the needle on such path is based on duty-cycle spinning. Minhas et al. (2007) showed that by duty-cycle spinning of the needle, paths with different curvatures can be achieved. In this method, the duty cycle, which determines the ratio between the simultaneous insertion and rotation time to the pure insertion time, is found as a function of the desired curvature. This method, however, requires the maximum value of the needle path curvature, which due to tissue inhomogeneity might be variable. Moreira et al. (2014a) have integrated online curvature estimation to 3D planners and duty-cycle spinning to overcome the

curvature uncertainties. Majewicz et al. (2014) present two strategies for duty-cycle spinning to overcome the hardware limitations such as cable windup.

There have been different techniques used in the literature for motion planning of the needles such as optimization-based methods, rapidly exploring random tree (RRT) algorithms, and inverse kinematics. In optimization-based methods, efforts are made to optimize a predefined cost function subject to obstacle and needle constraints. One main criterion in clinical procedures is to minimize the trauma imposed on the tissue and to avoid collisions with any sensitive tissues. To this end, the planning method can be formulated as an optimization problem subject to equalities and inequalities constraints. Different optimization methods are used to find the optimal path in the sense of path length, the number of rotations, and distance to the obstacles (Bobrenkov et al., 2014; Wang et al., 2014; Schulman et al., 2014).

The RRT algorithms use the fast exploring methods to find all the feasible points. The RRT algorithm is a randomized path planning method proposed specifically for nonholonomic systems. This method is based on searching the state space, excluding the states that lie in the obstacle regions. Due to the nonholonomic constraints and the maximum curvature of the needle, the reachable region of the needle is a mushroom-like area (Vrooijink et al., 2014), so not all the configurations are reachable from the current configuration. To overcome this limitation, different modifications have been made on the RRT algorithm and used for needle path planning (Vrooijink et al., 2014; Bernardes et al., 2011, 2013, 2014; Shkolnik et al., 2009; Patil and Alterovitz, 2010).

The inverse kinematics of the robotics manipulators determine the relation between the Cartesian space variables and the joint space (Craig, 2005). Similarly, for a bevel-tipped needle the inverse kinematics can be defined as the relation between the needle tip pose, that is, position and orientation, and the translation and orientation at the needle base. This method is usually employed along with other methods such as numerical calculations, space discretization, geometric methods, and optimizations (Duindam et al., 2010; Glozman and Shoham, 2004).

2.5 Control

There are two main differences between the needle steering control and motion planning. In control, the steering is performed in a closed-loop

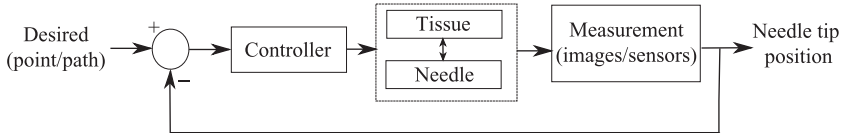


Fig. 3 Control loop for needle steering.

feedback structure. In this method, the controller calculates the control signal in real time based on the error, which is provided to the controller in the form of feedback, as shown in Fig. 3. However, unlike the motion planners that produce a sequence of control inputs for the current and future times, the controller only outputs the control action for the current time. Moreover, in planning methods, the errors caused by uncertainties and tissue non-homogeneity are compensated by replanning the desired path and the control sequence. In control, the desired input to the feedback loop is designed using any off-line path planner, whereas the controller is responsible for correcting the errors and steering the needle on the desired trajectory.

Due to the nonlinearity of the needle kinematics and dynamics, different control strategies such as model-based methods, probabilistic methods, and robust strategies have been applied to needle steering control. From a control perspective, in Haddadi et al. (2010), the controllability of the needle in soft tissue is studied using a dynamic model. Abolhassani et al. (2007) propose a method to perform the axial rotations when the needle deflection reaches some predefined threshold. In this method, the force data and the needle's model (flexible beam model) are employed to calculate the deflection and the rotation locations, and the goal is to keep the needle moving as straight as possible. Using a mechanics-based model of the needle, Khadem et al. (2016) developed a nonlinear model predictive controller for 2D needle steering, which is based on iterative optimization of the predictions. In Abayazid et al. (2013), fiber Bragg grating sensors are used to reconstruct the shape of the needle, which is used as feedback in the steering algorithm. The algorithm uses geometric methods to find the reachable regions and steers the needle such that the target lies in these regions. Considering the probabilistic approaches, Sovizi et al. (2016) propose a planner for 2D environment with obstacles using linear programming (LP). In this method, the uncertain system is approximated by a chain of discrete Markov process, considering the stochastic tissue motion. The optimal solution to this LP problem is found by minimizing the expectation of the cost function. Van Den Berg et al. model the needle motion and the sensor noise as a

stochastic process and use linear quadratic Gaussian optimization to obtain a minimal probability of intersection with obstacles. Due to the nonlinearity of the equations, this method linearizes the model around the path and controls the deviation from the that. In this work, different paths are found, from which the optimal one that minimizes the probability of intersections with obstacles is selected. The path is then implemented by duty-cycle spinning. Approximating the probability density function of the needle as a Gaussian variable, Park et al. (2010) use a path planning-based method for steering through intermediate steps using the path of probability algorithm. At each step, the position of the needle is compared to the desired intermediate step and the next step is determined to maximize the probability that next points reach the target.

2.5.1 Sliding mode control in needle steering

Sliding mode control (SMC) is a technique, suitable for systems with disturbances and uncertainties. This method provides a robust approach for reaching the desired performance (Dodds et al., 2015). This is a discontinuous method, in which the control input switches between two limits. If the system under control is of degree n , the SMC redefines the problem as stabilizing a differential equation $S(h^{-1}(y, \dot{y}, \dots, \dot{y}^{(n-1)}), y_d)$ of order $n - 1$, which is a relation between the system output and its derivatives. Here, h is the function relating the system states to the output y and y_d is the desired output value. The desired performance of the closed-loop dynamics is expressed as $S = 0$, which happens by proper design of the controller. The method proposed in Rucker et al. (2013) is a sliding-based method, where the measurements from a five-DOF magnetic tracking sensor are combined with a Kalman filter to estimate the full needle tip orientation. This information is then used to express the Cartesian position error in the needle tip frame. Based on the error, the sliding mode controller constantly rotates the needle and moves it on a helical path to reach the desired target. In the sequel, sliding-based methods are presented, which only require the needle tip position measurement.

For the system equations (4), the sliding functions along x - and y -axes, S_i , ($i = x, y$), can be defined as

$$S_i = b\dot{e}_i + ce_i \quad (i = x, y) \quad (11)$$

in which $e_x = x - x_d$ and $e_y = y - y_d$. In this function, b and c are constant coefficients, which determine the convergence rate of the error and x_d and y_d

are the desired position along the x - and y -axes, respectively. If x_d and y_d are constant, their first and second time derivatives equal zero, which simplifies the time derivative of Eq. (11) as $\dot{S}_x = b\ddot{x} + c\dot{x}$ and $\dot{S}_y = b\ddot{y} + c\dot{y}$. Consider the Lyapunov function $V_i = \frac{1}{2}S_i^2 (i = x, y)$. The goal is to find the control input such that $\dot{V}_i = S_i \dot{S}_i < -\eta |S_i|$, which leads to S_i , or equivalently, the error along the desired axes approach zero.

2.5.2 2D switching control

Consider the planar control of the needle, using the Y - Z deflection equation (7) and the two possible inputs for the bevel orientation. It is required to have

$$\begin{cases} \dot{S}_y > \eta & \text{if } S_y < 0 \\ \dot{S}_y < -\eta & \text{if } S_y > 0 \end{cases} \quad (12)$$

Using the assumption in Section 2.2, stating that $|\alpha| < \alpha^*$ with $0 < \alpha^* < \pi/4$, the sign of the first term in \dot{S}_y only depends on the bevel orientation. If b and c are selected such that

$$\frac{b\kappa\nu}{c} > \tan \alpha^* \quad (13)$$

then by selecting $+\kappa$ when $S_y < 0$, and $-\kappa$ when $S_y > 0$, Eq. (12) is satisfied. This means that every time S_y changes sign, the needle should rotate to change the bevel orientation. As a result, when S_y is close to zero, chattering may happen, which increases tissue trauma. To prevent such behavior, the switching can be performed using the switching threshold S_s as shown in Table 1. A smaller switching threshold is beneficial in having smaller errors; however, it increases the number of rotations. Details about selecting the switching threshold can be found in Fallahi et al. (2016b).

Table 1 Selection of the operating mode based on S_y .

| Region | System mode | $sign(\dot{S}_y)$ |
|--------------------------|-------------------------|-------------------|
| $S_y < -S_s$ | Mode 1 ($\kappa > 0$) | + |
| $-S_s \leq S_y \leq S_s$ | No mode change | + or - |
| $S_y > S_s$ | Mode 2 ($\kappa < 0$) | - |

2.5.3 Three-dimensional sliding mode control

In order to extend the 2D method presented in the previous section to 3D environment, two sliding functions are considered and combined for compensating the error in the 3D space. The sliding functions S_x and S_y are defined using Eq. (11) for constant values of x_d and y_d with $c = 1$. Taking the time derivative of the sliding functions and substituting from Eq. (6) gives

$$\dot{S}_x = b_x \kappa \nu^2 \cos \beta \sin \gamma + \nu \sin \beta \quad (14)$$

$$\dot{S}_y = -b_y \kappa \nu^2 \cos \alpha \cos \gamma - b_y \kappa \nu^2 \sin \beta \sin \alpha \sin \gamma + \nu \cos \beta \sin \alpha \quad (15)$$

Considering the x -direction, there are two terms on the right-hand side of Eq. (14). If the absolute value of the first term is greater than the second term, that is, $|b_x \kappa \nu^2 \cos \beta \sin \gamma| > \nu \sin \beta$, the first term determines the sign of \dot{S}_x . According to Eq. (5), since $\cos \beta > 0$, using $\kappa > 0$ and $\nu > 0$, this condition can be written as

$$|\sin \gamma| > \frac{1}{b_x \kappa \nu} |\tan \beta| \quad (16)$$

Similarly, for the y -axis, if

$$|\cos \gamma| > |\sin \beta \tan \alpha \sin \gamma| + \frac{1}{b_y \kappa \nu} |\cos \beta \tan \alpha| \quad (17)$$

the term $-\text{sgn}(\cos \gamma)$ determines the sign of \dot{S}_y . Similar to the 2D case, according to $\text{sgn}(\sin \gamma)$ and $\text{sgn}(\cos \gamma)$, there are two possibilities for each direction, leading to the total number of four possibilities (four quadrants) for the 3D case, as shown in Fig. 4. For example, if $S_x > 0$ and $S_y < 0$ require $\dot{S}_x < 0$ and $\dot{S}_y > 0$, which is equivalent to $\sin \gamma < 0$ and $\cos \gamma < 0$, or having γ in the third quadrant. This can be written as

$$\gamma_d = \text{atan2}(-S_x, S_y) \quad (18)$$

In this equation, $\gamma_d \in [-\pi, \pi]$ is the desired roll angle and the function atan2 represents the tangent inverse function considering the sign of the two inputs to return the appropriate quadrant of the calculated angle. However, this is only true if Eqs. (16), (17) are satisfied. To ensure this, the parameters can be selected for the worst-case scenario. Using the assumption $|\alpha| < \alpha^*$ and $|\beta| < \beta^*$, Eqs. (16), (17) can be combined as

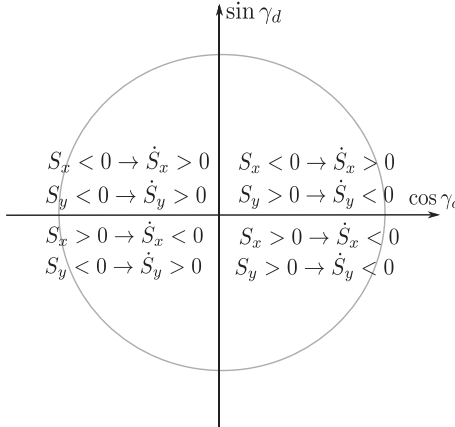


Fig. 4 The corresponding quadrant for γ_d based on $\text{sgn}(S_x)$ and $\text{sgn}(S_y)$.

$$\begin{aligned} \arcsin\left(\frac{1}{b_x \kappa \nu} \tan \beta^*\right) &< |\gamma_d| \\ &< \arccos\left(\sin \beta^* \tan \alpha^* + \frac{1}{b_y \kappa \nu} \cos \beta^* \tan \alpha^*\right) \end{aligned} \quad (19)$$

in which α and β are substituted by α^* and β^* , respectively. This inequality gives the criteria for selecting the design parameters b_x and b_y . According to the definition of S_i ($i = x, y$), smaller values of b_i are more desirable for having faster convergence; however, this will force α^* and β^* to be small, limiting the reachable workspace. From Eq. (19), it is clear that b_x , b_y , α^* , and β^* all affect the acceptable value of γ_d . The control input can be found by controlling the angle γ to the desired value γ_d in Eq. (18).

Note that since the needle system does not have any equilibrium points, the controller can only keep the sliding function very close to zero, because as long as the needle is moving the time derivative of the states changes. One way to deal with this property is to focus just on the deflection error and not on its time derivatives. This can be done by using a rotating sliding function, as shown in Fig. 5. The sliding surface (11) defines a line in the phase plane and can be rotated about the origin by changing the slope of the line $\frac{1}{b_i}$ ($i = x, y$). In Fig. 5, as the sliding function is rotated toward the vertical axis, the error decreases. The sliding function with variable slope is written as

$$\dot{S}_i = b_i \ddot{e}_i + \dot{e}_i (\dot{b}_i + 1), \quad i = x, y \quad (20)$$

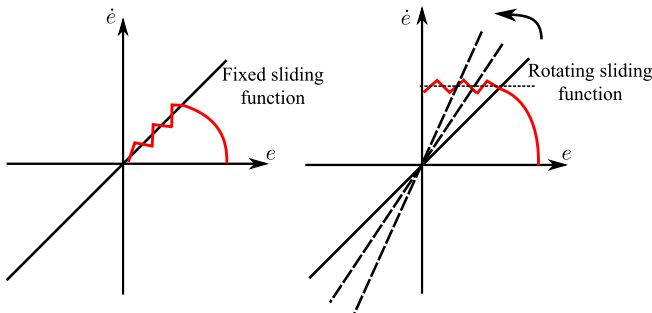


Fig. 5 Phase plane representation of the fixed and rotating sliding functions.

Selecting $b_i = -1$ gives

$$\dot{S}_x = b_x \kappa v \cos \beta \sin \gamma \quad (21)$$

$$\dot{S}_y = -b_y \kappa v \cos \alpha \cos \gamma + b_y \kappa v \sin \beta \sin \alpha \sin \gamma \quad (22)$$

Since b_i ($i = x, y$) should be positive, the initial condition $b_i(0)$ is selected such that $b_i(0) \geq \frac{D}{v}$, where D is the final insertion depth and v is the insertion velocity. This structure relaxes the constraint (19) as

$$|\tan \gamma_d| < \frac{1}{\sin \beta^* \tan \alpha^*} \quad (23)$$

in which there is no dependence on the needle path curvature κ . Using the rotating sliding function, b_i gets smaller with time, which increases the weight of the position error in the sliding function, leading to smaller errors. The stability proof of this method and more details are provided in Fallahi et al. (2017).

2.5.4 PWM switching and sliding mode control

The application of the sliding mode technique for needle steering is not limited to the methods mentioned earlier. In the following, the application of SMC in an averaged model of the needle steering system is presented. The average-based structure models the 3D needle steering system as a four-mode switching system to transform the continuous input into a switching sequence. In this structure, the 3D system is divided into two 2-mode switching subsystems. Assuming the switching is performed in a pulse width modulation (PWM) structure, the time averaged of each subsystem across the PWM period represents the original subsystem. For each subsystem, a virtual input is defined, which can be designed individually and gives the

duty cycle of switching for the subsystem. The duty cycles from both subsystems are then combined to steer the needle in the 3D space. Here, the sliding mode technique is used for designing the controllers for each subsystem, which shows another application of sliding mode technique in the context of needle steering.

The time-averaged model is given by [Fallahi et al. \(2018\)](#)

$$\ddot{x}_a = d_x b_x |\bar{u}_x| - (1 - d_x) b_x |\bar{u}_x| = b_x u_x \quad (24a)$$

$$\ddot{y}_a = d_y (f_y + b_y |\bar{u}_y|) + (1 - d_y) (f_y - b_y |\bar{u}_y|) = f_y + b_y u_y \quad (24b)$$

with

$$u_x = (2d_x - 1) |\bar{u}_x| \quad (25a)$$

$$u_y = (2d_y - 1) |\bar{u}_y| \quad (25b)$$

where $b_x = \kappa v^2 \cos \beta$, $f_y = \kappa v^2 \sin \alpha \sin \beta \sin \gamma_d$, $b_y = -\kappa v^2 \cos \alpha$, $\bar{u}_x = \sin \gamma_d$, and $\bar{u}_y = \cos \gamma_d$. The angle γ_d is the desired roll angle, which for each direction, can take only two fixed values (modes) separated by 180 degrees, such that $\gamma_d \in [0, \pi]$ for the x -axis and $\gamma_d \in [-\pi/2, \pi/2]$ for the y -axis. The previous equations are found with the assumption that the switching between these two modes is performed according to the normalized PWM period $D_i = [d_i \ 1 - d_i]$ with $\|D_i\| = 1$ ($i = x, y$). Here, u_x and u_y are the virtual inputs for the subsystems, which should be designed properly. Regardless of the method used in designing these control signals, these values can be converted into the duty cycles d_x and d_y to determine the duty cycle of switching between the two modes as

$$d_i = \frac{(u_i / |\bar{u}_i| + 1)}{2} \quad i = x, y \quad (26)$$

Since \bar{u}_x and \bar{u}_y are related to $\sin \gamma_d$ and $\cos \gamma_d$, respectively, it is possible to integrate the two 2-mode subsystems to build up a four-mode composite system. These four modes are selected based on the sign of $\sin \gamma_d$ and $\cos \gamma_d$, as shown in [Fig. 6A](#). Through this selection, if $|\tan \gamma_d| = 1$, equal weights are given over the x - and y -directions. This weighting can be changed by selecting $|\tan \gamma_d| > 1$ or $|\tan \gamma_d| < 1$. The switching pattern is shown in [Fig. 6B](#).

In this formulation, u_x and u_y can be designed using different control strategies and then transformed into the duty-cycle variables d_x and d_y to be used in the 3D switching framework. In the sequel, the sliding mode technique is used for designing the control signals u_x and u_y , which provides

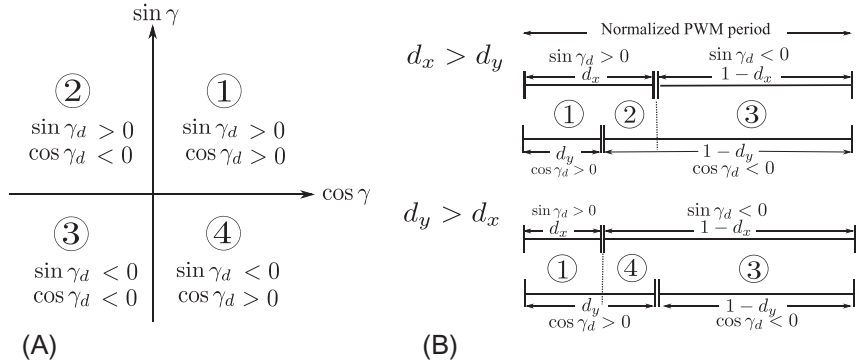


Fig. 6 The four-mode switching pattern. (A) The half plane modes for each subsystem and the resultant four modes: ① $\sin \gamma_d > 0, \cos \gamma_d > 0$, ② $\sin \gamma_d > 0, \cos \gamma_d < 0$, ③ $\sin \gamma_d < 0, \cos \gamma_d < 0$, ④ $\sin \gamma_d < 0, \cos \gamma_d > 0$. (B) The switching pattern when $d_x > d_y$ and $d_y > d_x$.

a suitable solution to deal with parameter uncertainties and disturbances. Moreover, due to the lack of proper measurements of the angles α and β their uncertainties should be considered in the equations. The terms dependent on these angles appear as bounded trigonometric functions, for which their bounds can be used to define the nominal and uncertain systems. Using the bounds on the needle curvature and the orientation-related terms, the bounds on b_x and b_y can be written as

$$\underline{\kappa} \nu^2 \cos \beta^* \leq b_x \leq \bar{\kappa} \nu^2 \quad (27a)$$

$$\underline{\kappa} \nu^2 \cos \alpha^* \leq b_y \leq \bar{\kappa} \nu^2 \quad (27b)$$

Assuming $\hat{\kappa}$, \hat{b}_x , and \hat{b}_y as the nominal values of the parameters defined by the geometric mean of the previous bounds as $\hat{\kappa} = \sqrt{\underline{\kappa} \bar{\kappa}}$, $\hat{b}_x = \hat{\kappa} \nu^2 \sqrt{\cos \beta^*}$, and $\hat{b}_y = -\hat{\kappa} \nu^2 \sqrt{\cos \alpha^*}$, the nominal subsystems can be written as

$$\ddot{\hat{x}}_a = \hat{b}_x \hat{u}_x \quad (28)$$

with

$$\left(\frac{\underline{\kappa} \cos \beta^*}{\bar{\kappa}} \right)^{1/2} \leq \frac{\hat{b}_x}{b_x} \leq \left(\frac{\bar{\kappa} \cos \beta^*}{\underline{\kappa}} \right)^{1/2} \quad (29)$$

Similarly, the nominal subsystem in the γ -direction can be written as

$$\ddot{\hat{y}}_a = \hat{f}_\gamma + \hat{b}_y \hat{u}_\gamma \quad (30)$$

with

$$|\hat{f}_y - f_y| \leq 2\bar{\kappa}v^2 \quad (31a)$$

$$\left(\frac{\underline{\kappa} \cos \alpha^*}{\bar{\kappa}}\right)^{1/2} \leq \frac{\hat{b}_y}{b_y} \leq \left(\frac{\bar{\kappa} \cos \alpha^*}{\underline{\kappa}}\right)^{1/2} \quad (31b)$$

Consider the sliding function (11) for the y -direction with $b = 1$. Taking its time derivative gives

$$\dot{S}_y = f_y + b_y u_y - \ddot{y}_d + c \dot{e}_y \quad (32)$$

Using Eq. (30) and solving for $\dot{S}_y = 0$ the control law u_y is found as

$$\hat{u}_y = \frac{1}{\hat{b}_y} \left(-\hat{f}_y + \ddot{y}_d - c \dot{e}_y \right) \quad (33)$$

Similarly for the x -direction

$$\hat{u}_x = \frac{1}{\hat{b}_x} (\ddot{x}_d - c \dot{e}_x) \quad (34)$$

However, these control signals only work for the nominal subsystems. Using the Lyapunov function $V_i = \frac{1}{2} S_i^2$ ($i = x, y$), in Fallahi et al. (2018) it is shown that the following controllers ensure the convergence of the uncertain system:

$$u_x = \hat{u}_x - \frac{1}{\hat{b}_x} K_x \operatorname{sgn}(S_x) \quad (35a)$$

$$u_y = \hat{u}_y - \frac{1}{\hat{b}_y} K_y \operatorname{sgn}(S_y) \quad (35b)$$

with

$$K_x = \lambda_x \eta + (\lambda_x - 1) |\hat{b}_x \hat{u}_x| \quad (36a)$$

$$K_y = \lambda_y (F_y + \eta) + (\lambda_y - 1) |\hat{b}_y \hat{u}_y| \quad (36b)$$

where $\lambda_x = \left(\frac{\bar{\kappa} \cos \beta^*}{\underline{\kappa}}\right)^{1/2}$, $\lambda_y = \left(\frac{\bar{\kappa} \cos \alpha^*}{\underline{\kappa}}\right)^{1/2}$, $F_y = 2\bar{\kappa}v^2$, and $\eta > 0$.



3 Beating-heart surgery

Beating-heart surgery has significant advantages over conventional arrested-heart surgery. However, the fast motion of the beating heart introduces a challenge to the surgeon (human operator). To overcome this obstacle, a mechanical heart stabilizer ([Bachta et al., 2009b](#)) is usually used to keep the beating heart from moving. However, this device can only reduce the motion in a localized area on the exterior surface of the beating heart. To minimize the risks of tool-tissue collision and tissue injury, a robot-assisted system is necessary to automatically provide compensation for the fast beating heart's motion, so that to assist the human operator to perform operation accurately and precisely. Indeed, if the robotic system can move a surgical tool in synchrony with the target tissue while the heart beats, the oscillatory forces between the surgical tool and heart tissue may be small, and the human operator can then perform the surgical procedure as if the beating heart is stationary.

The robot-assisted system, however, introduces another issue: haptic feedback. As the human operator cannot make contact with the surgical tool, the tool-tissue interaction forces cannot be perceived by the human operator directly. To provide haptic feedback to the human operator, in some robot-assisted systems, a force sensor is attached to the end of the surgical robot to register forces. When the surgical robots' motions are synchronized with the hearts motions, the force sensor inertia will cause oscillatory forces, which should not be transmitted to the human operator. In other words, the haptic feedback should only contain the nonoscillatory portion of the environmental forces. To date, the state-of-the-art research on robot-assisted beating-heart surgical systems has been studied to compensate for the hearts motion and reflects nonoscillatory haptic forces to the human operator.

3.1 Related work

Depending on the intended surgical procedures, several robot-assisted surgical systems have been developed, which can be mainly categorized into two groups based on the interaction modes with the human operator ([Tavakoli, 2008](#)): handheld surgical robotic systems and teleoperated surgical robotic systems.

Handheld surgical systems require the human operator to hold the surgical system directly, which includes an actuator and a surgical tool attached

at the end of the system so that the surgical tool can move with respect to the handle (Kettler et al., 2007; Yuen et al., 2009; Zahraee et al., 2010).

Different from the handheld surgical systems, a teleoperated surgical system involves a master robot that provides position and/or force commands and a slave robot that receives those commands and executes tasks on the heart tissue (Bowthorpe et al., 2014a, b). These systems have been shown to offer lots of advantages such as dexterity, fine and remote manipulation capability, and haptic feedback capability for the human operator. The DaVinci surgical robotic system (Guthart and Salisbury, 2000) by Intuitive Surgical Inc. (Sunnyvale, California, United States) is one of the most prominent commercial teleoperated surgical systems.

Teleoperated surgical systems can be divided into two categories depending on their features. In a unilateral teleoperation system, the human operator loses the sense of touch. In contrast, in a bilateral teleoperation system, the human operator can feel the interaction force between the slave robot and what it is touching, enabling the human operator to efficiently manipulate the master robot to provide appropriate commands.

Conventional surgical tools used in robot-assisted systems for cardiac surgeries are short and rigid. Surgical tools like scissors, forceps, and graspers are usually mounted on the end of the systems to perform surgical tasks. However, during intravascular interventions and minimally invasive surgeries, the dexterity of surgical robots can be enhanced by using flexible, thin, and lightweight surgical tools such as catheters while also reducing trauma, which is a benefit for postoperative recovery (Tavakoli et al., 2007). These flexible surgical tools can be combined with the above robot-assisted systems to perform intended surgical procedures (Kesner and Howe, 2011b; Khoshnam and Patel, 2017).

3.2 Measurements and feedbacks

To address the issue of beating-heart motion compensation, several types of sensors have been used to capture the position of the heart, so that the human operator perceives visual feedback of the surgical site through sensors, and the robotic surgical instruments track the beating heart's motion by utilizing the measured heart positions.

Nakamura et al. (2001) adopted one color camera to provide colorful visual feedback and one monochrome high-speed camera to measure the heart position. The human operator utilized the guidance of those two cameras to demonstrate automatic tracking of a point on the heart that was lit by

laser. Ginhoux et al. (2004, 2005) and Gangloff et al. (2006) measured the 2D cardiac motions by using a 500-Hz camera to avoid aliasing. Richa et al. (2010, 2011) and Yang et al. (2015) extended 2D position tracking to 3D position tracking using a stereo camera system. In addition, the high-speed camera has been employed in other literatures about beating-heart surgery as well (Bachta et al., 2009a, 2011; Nakajima et al., 2014; Ruszkowski et al., 2016). These sensors provided real-time and accurate position information to compensate for the rapid movement of the beating heart. However, high-speed cameras can only visualize the outer surface of the heart and are not appropriate for surgeries performed inside the heart.

In Schweikard et al. (2000), a pair of X-ray cameras and an infrared tracking system were combined to obtain the positions of the internal markers attached to the heart tissue. Similarly, Mansouri et al. (2018) used an infrared tracker system to locate the 3D positions of the heart. These methods require passive markers attached on the point of interest of the heart tissue, which may be affected during tool-tissue interaction and further operations.

Another common sensor used for guiding intracardiac beating-heart repairs is US machine. Yuen et al. (2008, 2009) developed a 3D US-guided motion compensation system for beating-heart mitral valve repair. Kesner and Howe (2014) applied a robotic catheter system combining US guidance and force control to perform cardiac tissue ablation. Bowthorpe and Tavakoli (2016a, b, c) and Cheng and Tavakoli (2018b) developed a master-slave teleoperated system and combined US images with various controllers to compensate for the beating heart's motion. The acquisition and processing of US images cause a large time delay, which needs to be compensated for via control.

In addition to various image-based sensors, nonimage-based sensors such as force sensors and sonomicrometry crystals are proposed to solve the problem of motion compensation and/or haptic feedback.

Moreira et al. (2012, 2014b), Dominici and Cortesao (2014a, b), and Cortesao and Dominici (2017) utilized force sensors to compensate for the physiological motion by controlling the contact forces to track the desired ones. These methods were assumed that the surgical robot has somehow been initially controlled to come into contact with the heart tissue, and the control goals are maintaining contact between the tool and the tissue.

Tuna et al. (2013) and Bebek and Cavusoglu (2007) used sonomicrometry crystals to track the beating-heart motion in real time and generalized adaptive predictors to predict the hearts motion. By putting six and one sonomicrometry crystals under and on the surface of the heart, the

electrocardiogram (ECG) biological signals of the heart surface can be measured based on the transmission and reception of US signals. This technique is feasible as the heart position can be captured through blood, although the calculation is complex and time consuming.

3.3 Control

Various position-, force-, and impedance-based control methods have been proposed for enabling tool-tissue motion compensation for beating-heart surgery and nonoscillatory haptic feedback in teleoperation systems.

3.3.1 Position-based control methods

The position-based controllers need the current beating heart's position and can be classified into predictive feed-forward controllers and predictive feedback controllers. Predictive feed-forward controllers use the heart's position as the set point to move the surgical tools. Predictive feedback controllers not only need the heart's current position but also take the tracking error into account.

[Bebek and Cavusoglu \(2007\)](#) proposed a control algorithm based on the previous quasiperiodic heart motions which are ECG signals detected through sonomicrometry crystals. [Yuen et al. \(2009\)](#) collected the heart positions from US images, and employed an extended Kalman filter (EKF) to compensate the time delay caused by image acquisition and processing. This method took advantage of the quasiperiodicity of the heart motion and modeled the heart motion as a time-varying Fourier series. Many of the predictive feed-forward controllers are used for handheld systems.

To further compensate for the position tracking errors, predictive feedback controllers are used. [Bowthorpe et al. \(2014b\)](#) developed a teleoperation system and proposed a feedback controller with a modified Smith predictor to ensure the distance between the surgical tool and the heart at desired values as commanded by the human operators hand position. [Bowthorpe and Tavakoli \(2016c\)](#) presented three different Smith-predictor-based feedback controllers to tackle issues such as time delays, different measurement rates, and unregistered sensor data.

3.3.2 Force-based control methods

Force control methods are benefit for applications that require contact such as heart biopsy with controlled depth. Considering the process of tool-tissue interaction in robot-assisted beating-heart surgery, precisely applying forces on the beating-heart tissue and enabling the surgical robot to comply with

the beating heart's motion simultaneously is important. Therefore, several force control methods were proposed.

Moreira et al. (2012, 2014b) proposed a force control method using active observer based on a viscoelastic interaction model to compensate for the physiological motion. Dominici and Cortesao achieved motion compensation by designing a cascade model predictive control architecture with a Kalman active observer (Dominici and Cortesao, 2014a, b), and a double active observer architecture (Cortesao and Dominici, 2017). These systems use similar feedback controllers. In addition, Yuen et al. (2010) and Kesner and Howe (2011a, 2014) separately combined the US image guidance with a force controller incorporating a feed-forward term containing the estimated motion of the beating heart. These methods incorporated position control and force control to achieve beating-heart motion compensation.

Much of the earlier work focus on handheld systems instead of teleoperation systems, which are possible to enable haptic feedback to the human operator. Haptic feedback during a surgical operation is significant for the human operator to be able to accurately execute the surgical tasks especially in beating-heart surgeries involving tissue cutting and sewing, grasping, dissection, etc. (Wagner et al., 2007). During the operation of such surgical tasks, the tool-tissue interaction forces should be within a safety range to avoid potential tissue injury. To enable the human operator to perceive appropriate haptic feedback under contact, bilateral teleoperation systems were studied. As discussed earlier, the issue of oscillatory haptic feedback caused by force sensor inertia should be considered. For instance, Nakajima et al. (2014) performed haptic feedback using an acceleration-based bilateral control system. Moharer et al. (2014) developed a force feedback control system for bimanual telerobotic surgery using the DaVinci surgical system (Intuitive Surgical Inc., Sunnyvale, California, United States).

3.3.3 Impedance-based control methods

Most successful applications of robot-assisted surgical systems to date have been performed based on the position or force control, in which the surgical robot is treated essentially as an isolated system. However, in robot-assisted beating-heart surgeries, control of the dynamic behavior between the surgical robot and the beating-heart tissue is also required. Given the beating heart contains inertial objects, the surgical robot and the beating heart can be expressed as an impedance and admittance, respectively (Hogan, 1984, 1985). Generally, the beating heart can be regarded as a source of

disturbances “to the surgical robot, and the disturbance response” of the surgical robot can be modulated to control the dynamic behavior between the surgical robot and the beating-heart tissue by varying the parameters and/or structure of the impedance.

Zarrouk et al. (2010) proposed an adaptive control architecture based on the model reference adaptive control to solve the 3D physiological motion compensation in beating-heart surgery. A reference impedance model and an adaptive controller were designed for the surgical robot. In Cheng and Tavakoli (2018a, b), Sharifi et al. (2018), and Cheng et al. (2018), the model reference adaptive control was applied to a bilateral teleoperation system. The authors designed two reference impedance models for the master and slave robots to simultaneously make the slave robot compensate for the heart motion and ensure the human operator to perceive nonoscillatory haptic feedback. The main advantage of impedance-based control system is the desired performance can be achieved via appropriate parameter adjustment of the reference impedance models without any measurement or estimation of the beating heart’s motion. In the following, two reference impedance model-based teleoperation systems are presented to describe the applications of observation and feedback control in robotic systems for beating-heart surgery.

Bilateral impedance control: The developed bilateral impedance-controlled teleoperation system is shown in Fig. 7. Here, f_h is the interaction force between the master robot and the human operator and f_e is the interaction force

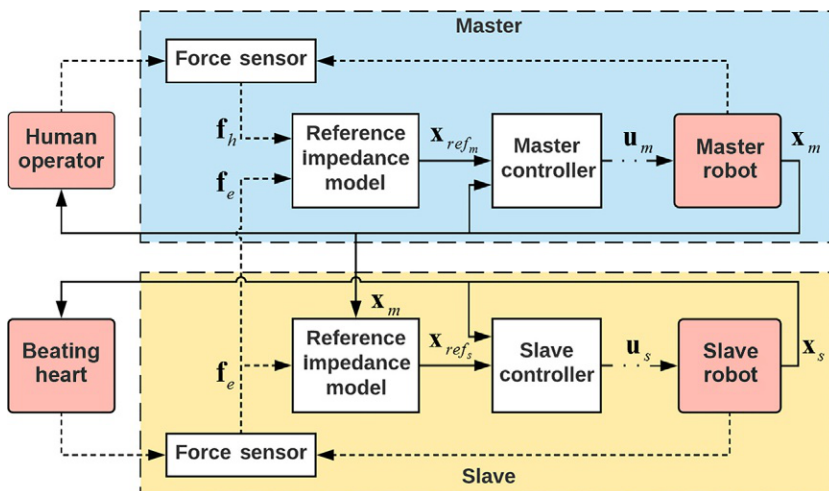


Fig. 7 The block diagram of the bilateral impedance-controlled teleoperation system with two reference impedance models for the master and slave robots.

force between the slave robot and the beating heart. They are measured directly through two force sensors. Also, \mathbf{x}_{ref_m} and \mathbf{x}_{ref_s} are the desired position for the master and slave robots and \mathbf{x}_m and \mathbf{x}_s are the actual position of the master and slave robots, respectively. The controllers receive the position errors between the desired positions generated by the reference models and the actual positions read from the robots and then output torque \mathbf{u}_m and \mathbf{u}_s to the robots.

The reference impedance models for the master and slave robots are designed and can be expressed as

$$m_m \ddot{\mathbf{x}}_{ref_m} + c_m \dot{\mathbf{x}}_{ref_m} + k_m \mathbf{x}_{ref_m} = \mathbf{f}_h - k_f \mathbf{f}_e \quad (37)$$

$$m_s \ddot{\tilde{\mathbf{x}}}_{ref_s} + c_s \dot{\tilde{\mathbf{x}}}_{ref_s} + k_s \tilde{\mathbf{x}}_{ref_s} = -\mathbf{f}_e \quad (38)$$

where $\tilde{\mathbf{x}}_{ref_s} = \mathbf{x}_{ref_s} - k_p \mathbf{x}_m$, and k_p is the position scaling factor. In the earlier, k_s , c_s and k_m , c_m , m_m are the virtual stiffness, damping, and mass parameters of the slave, and master impedance models, respectively. Also, k_f is the force scaling factor.

In order to accomplish the desired objectives, the parameters for the two reference impedance models should be adjusted appropriately. The damping ratios and the natural frequencies of the reference impedance models are introduced. Given one of the stiffness, damping, and mass parameters, the rest two parameters can be calculated through $\zeta_i = c_i / 2\sqrt{m_i k_i}$ and $\omega_{n_i} = \sqrt{k_i / m_i}$ ($i = m$ for the master, and $i = s$ for the slave). To ensure the impedance models have fast behaviors in response to the force inputs and small overshoots in response to the step force inputs, the damping ratios are set as 0.7.

The master impedance model (37) should be designed to provide feedback of the nonoscillatory part of the slave-heart interaction force for the human operator. For this purpose, the stiffness parameter (k_m) of the master impedance model should be chosen small, and the natural frequency of the master impedance model (ω_{n_m}) should be much lower than the frequency of the beating heart ω_h which has a range of 6.28–10.68 rad/s ($\omega_{n_m} \ll \omega_h$).

The slave impedance model (38) should be adjusted such that the slave robot complies with the physiological force during the interaction procedure. The stiffness of the slave impedance model (k_s) should be moderate as a too small value will lead to a super flexible slave robot and too large value will make the slave robot very rigid. The natural frequency of the slave impedance model (ω_{n_s}) should be much greater than the frequency of the heart ($\omega_{n_s} \gg \omega_h$). Detailed parameter adjustments can be found in

Table 2 Parameter adjustments of the master and slave impedance models

| Characteristics | Master impedance adjustment | Slave impedance adjustment |
|-------------------|--|---|
| Stiffness | $k_m = 5 \text{ N/m}$ | $k_s = 100 \text{ N/m}$ |
| Damping ratio | $\zeta_m = 0.7$ | $\zeta_s = 0.7$ |
| Natural frequency | $\omega_{n_m} = 0.5 \text{ rad/s}$ | $\omega_{n_s} = 50 \text{ rad/s}$ |
| Damping and mass | $m_m = 20 \text{ kg}, c_m = 14 \text{ Ns/m}$ | $m_s = 0.04 \text{ kg}, c_s = 2.8 \text{ Ns/m}$ |
| Scaling factor | $k_f = 1$ | $k_p = 1$ |

[Cheng et al. \(2018\)](#). The adjusted parameters of the two impedance models are listed in [Table 2](#).

By focusing on the direction of the major component of heart motion the proposed bilateral impedance-controlled teleoperation system (with motion compensation) was compared to the regular direct force reflection (DFR) teleoperation system (without motion compensation) ([Liu and Tavakoli, 2011](#)), which reflects the entire slave–heart contact force to the human operator and requires the operator to take care of the motion compensation manually. [Fig. 8](#) shows the positions and forces during slave–heart interaction.

Without motion compensation, it is difficult to synchronize the slave robot with the beating heart. Comparatively, with motion compensation, the oscillatory force of the moving tissue was filtered, and only a stable baseline contact force was perceived by the human operator. Also, the position deviation between the slave robot and the heart during contact was very small. The human operator was easier to perform tasks, and the human–master interaction forces were steady and small.

Ultrasound image guidance and robot impedance control: In the earlier, as the stiffness of the slave impedance model (k_s) is chose to be moderate, the force applied on the heart tissue will not be very large, which limits the system’s application. To this end, [Cheng and Tavakoli \(2018b\)](#) proposed that to combine the robot impedance control with US imaging algorithm to achieve the two objectives of the system ([Fig. 9](#)). The US imaging-based control algorithms are used to make motion compensation. The impedance model for the master robot is designed to provide the human operator with a feeling of operating on an idle heart.

In the slave site, an US imaging machine is used to obtain the position of the beating heart \mathbf{x}_e . The summed position of the master robot \mathbf{x}_m and the heart \mathbf{x}_e transmitted to the slave robot as a reference signal $\mathbf{x}_{ref.} (= \mathbf{x}_m + \mathbf{x}_e)$. And then a slave controller is used to make the position of the slave robot \mathbf{x}_s follow its reference trajectory $\mathbf{x}_{ref.}$. In the master site, the human–master interaction force f_h and the slave–heart interaction force f_e are transmitted directly to a reference impedance model, which as we discussed earlier

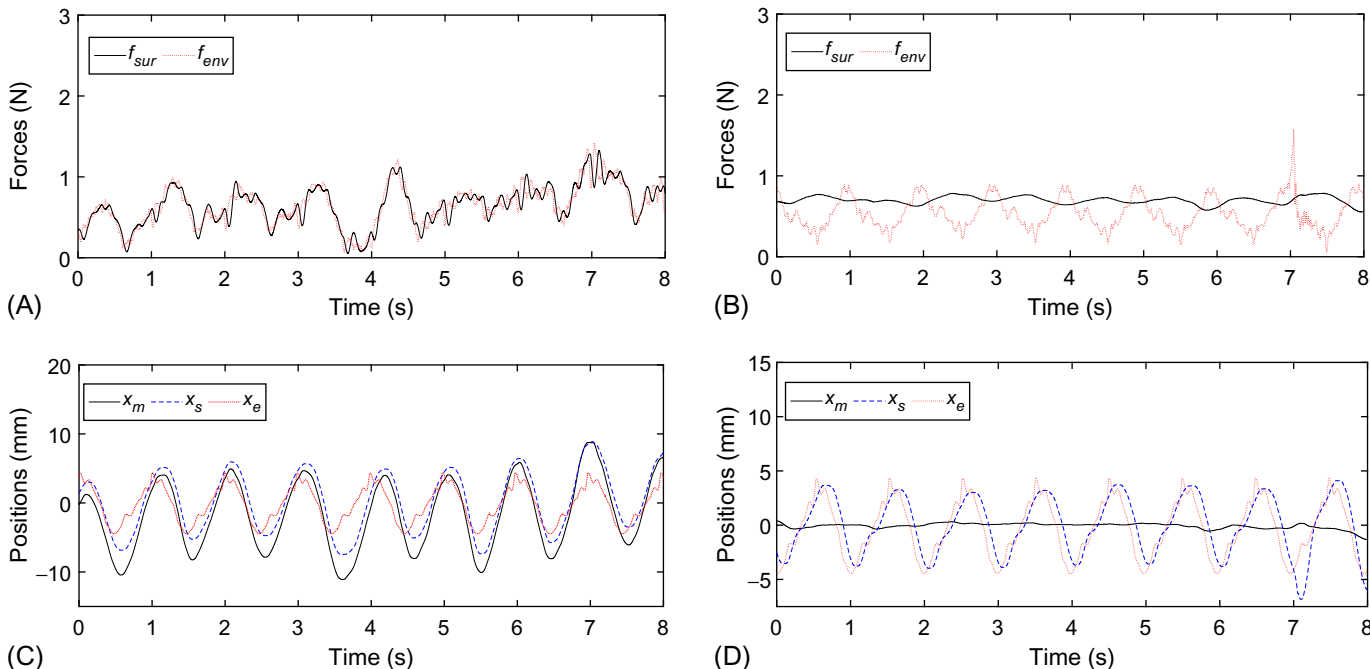


Fig. 8 Contact forces and positions (A), (C) without motion compensation, and (B), (D) with motion compensation.

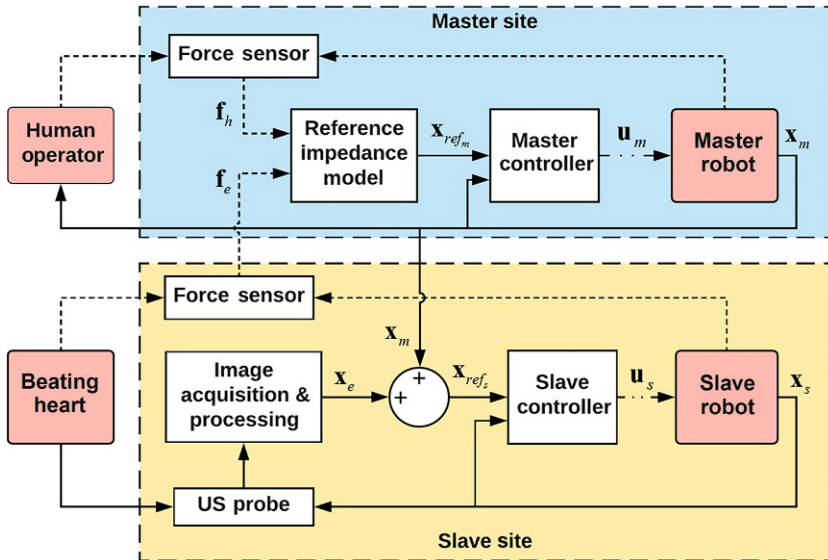


Fig. 9 The teleoperation system with US image guidance and robot impedance control.

can filter out the high-frequency portion of f_e and achieve f_h equals the filtered f_e . The impedance model generates a reference position x_{ref_m} for the master robot to follow.

For the sake of brevity, we will focus on the direction of the major component of heart motion. The motion compensation system is designed to make the slave robot to follow the combined trajectory of the master robot and the beating heart. The beating-heart position can be calculated based on the position of the slave robot and the measured robot-heart distance captured by US imaging along the surgical tools axis. The slow sampled robot-heart distance can be measured directly from each US image (the detailed algorithm is in Cheng and Tavakoli, 2018b). As the low sampling rate of the US image, the measured robot-heart distance needs to be upsampled to the system control sampling rate first by using cubic polynomial interpolation. Then, the delayed upsampled heart position can be obtained by delaying the position of the slave robot and adding it to the upsampled robot-heart distance. To further compensate for the time delay, the delayed quasiperiodic heart position is modeled as a time-varying Fourier series and predicted by an EKF. The reference impedance model for the master robot is designed the same as shown in the bilateral impedance control.

In experiments, the proposed method (Fig. 10C and F) was compared with the regular DFR teleoperation without and with automatic motion

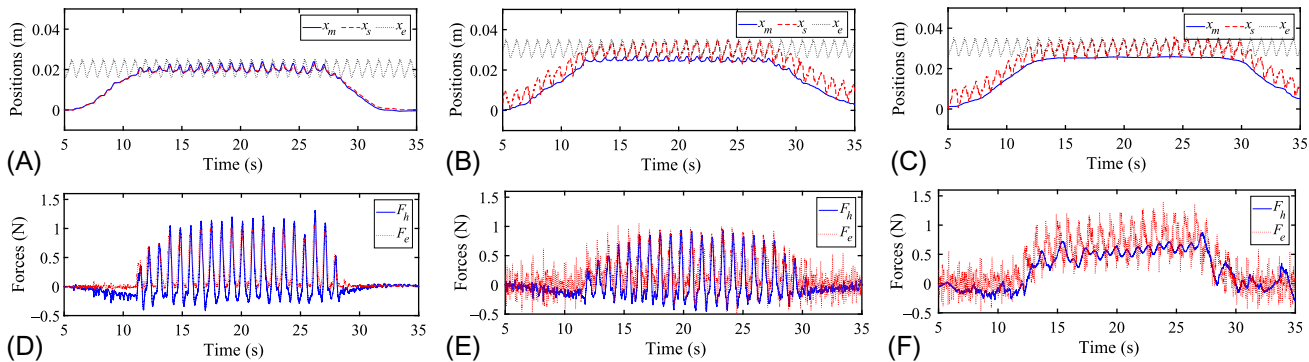


Fig. 10 Position and force results (A) and (D) for the DFR teleoperation system without AMC, (B) and (E) for the DFR teleoperation system with AMC, and (C) and (F) for the proposed teleoperation system.

compensation (AMC). The DFR teleoperation system without AMC ([Fig. 10A](#) and D) requires the human operator to perform motion compensation manually, while the DFR teleoperation system with AMC ([Fig. 10B](#) and E) compensates for the hearts motion automatically.

In [Fig. 10A](#) and D, the slave robot tracks both positions and forces of the master robot during the entire operation. However, the tracking of the beating-heart motion is poor as the human operator must manually compensate for the heart motion. Moreover, the oscillatory human–master interaction force suggests that the human operator receives unsteady haptic feedback, which makes it more challenging to synchronize the motion of the slave robot with the hearts motion. In [Fig. 10B](#) and E, the position tracking result is much better in this case than that in the first case. Nevertheless, the haptic feedback to the human operator is still oscillatory. An oscillatory motion with small amplitude remains in the master robot position due to the poor quality of haptic feedback. In [Fig. 10C](#) and F, the position tracking result is significantly better than that in [Fig. 10A](#) and D. Both the position and force of the master robot are much steadier as the oscillatory portions have been filtered using the proposed impedance model for the master robot. The human operator is able to operate on a beating heart without manual compensation, and simultaneously has a sense of operation on a seemingly idle heart.



4 Discussion

The discussion of this chapter is twofold: [Section 2](#) addresses the needle insertion procedures and [Section 3](#) discusses the challenges in beating heart surgery. The control strategies mentioned in [Section 2](#), show the application of the sliding mode control in needle steering. The 2D controller in [Section 2.5.2](#) is supplied with the needle deflection error obtained from ultrasound images and switches the system to the proper mode for reducing the targeting error. The constraints on switching parameters are derived using kinematic unicycle equations for the needle to ensure the stability of the system and convergence of the error. Similarly, the 3D controller in [Section 2.5.3](#) finds the desired value of the needle base angle to steer the needle on the desired path in the 3D environment and to reduce the number of rotations and the tissue trauma. In this method, for each sub-system, a sliding surface is defined, and the two sliding surfaces are combined. In these methods the controller is not dependent on the exact knowledge of the system parameters, and only the maximum value of the

needle path curvature is needed. These structures represent simple and non-model-based control strategies to improve needle tip positioning.

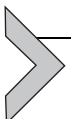
The sliding mode controller in [Section 2.5.4](#) is designed for a special framework, where the 3D needle equations are divided into two subsystems, representing the in-and out-of-plane motions. Each subsystem is considered as a planar switching system with two modes determining the two possible bevel orientations, which are 180 degrees apart. Assuming the switching between the two modes is performed according to some duty cycle period in a PWM framework, the performance of each subsystem is approximated by the averaged subsystem in the PWM period. Each averaged subsystem has its virtual input, for which controllers are designed using sliding mode control technique.

These mentioned methods use the position data obtained from ultrasound images. However, since the path traveled by the needle depends on the needle tip orientation, having information about the needle tip orientation will be helpful in the controller design process. Due to the small diameter of the needle and the low resolution of the images, it is not possible to retrieve the orientation information from the ultrasound images. This problem is dealt with by using state observers as explained in [Section 2.3](#), where linear and nonlinear observers are introduced for estimating the needle tip orientation. In this method, nonlinear transformations are applied on a 3D unicycle model. Since these equations do not satisfy the Lipschitz continuity condition, designing a convergent observer is not possible. Further studies are required in this field for designing nonlinear observers and their stable combination with controllers.

Regarding the beating heart surgery, in [Section 3](#), two impedance-based teleoperation systems were presented to achieve heart motion compensation and nonoscillatory robot-heart interaction feedback simultaneously. The bilateral impedance-controlled teleoperation system designed two reference impedance models for the master and slave robots, respectively. By tuning the parameters of the impedance models, the slave robot was able to comply with the movement of the beating heart, and the oscillatory portion of the slave-heart interaction force was filtered out, which made the human operator only perceive the nonoscillatory contact force. In the experiments, compared to the conventional DFR teleoperation system, the proposed system was able to provide the human operator a feeling of operating on an arrested heart and make the anchor deployment task much easier to perform. It should be noted that for the parameters of the slave robot's impedance model, they were adjusted to be moderate because too small values would

not apply enough forces to the heart and too large values would lead to the motion compensation be inaccurate. Therefore, this system is more suitable for surgeries that require less slave–heart contact forces such as mitral valve annuloplasty, blunt resection, ablation, etc.

To extend the applications for beating–heart surgery, the robot impedance control was combined with US image guidance, and the second system was proposed. This teleoperation system retained the reference impedance model for the master robot to attain nonoscillatory force feedback but replaced the reference impedance model for the slave robot with US image guidance for position control purposes. In this system, the slave robot provided motion compensation for the heart motion by following the position of the heart which was measured through US images. The low frame rate and time delay caused by image acquisition and processing were addressed by cubic polynomial interpolation and EKF, respectively. As the reference trajectory for the slave robot is the sum trajectory of the master robot and beating heart, large slave–heart contact force can be exerted on the heart tissue by increasing the master robot’s position commands. Consequently, the applications of this system can be extended to surgeries that need large slave–heart contact forces such as tissue cutting, penetration, and so on.



5 Conclusion

The subsections in [Section 2](#) provided an overview of the related observer and controller methods proposed for robot-assisted, image-guided needle steering. The goal of these approaches is to improve the needle tip positioning and increase the efficiency of the clinical needle insertion procedures. From the control perspective, the main challenges in designing a controller for needle/tissue system arise from the under-actuation property and the nonholonomic constraints imposed on the needle kinematics. Moreover, due to the small diameter of the needle and the low resolution of the ultrasound images, it is not possible to retrieve the orientation information from the ultrasound images, which can be dealt with by using state observers. The proposed control methods can be further expanded to have moving targets and obstacles, online estimation of the system parameters and observer/controller combination for trajectory tracking in the 3D environment. Further developments and experiments are required to verify the application of the proposed structures in clinical settings.

In [Section 3](#), another application of robotic assistive systems in beating–heart surgery is discussed. A robot-assisted beating–heart surgical system has

the potential to improve the outcome of many surgical procedures performed on the heart. There are different ways to control such a system as each surgical procedure has different requirements. For instance, the procedure could be ablation which requires small exerted force or tissue cutting which requires large exerted force. This would affect the choice of the motion-capture module and, in turn, affects the choice of a controller. Based on the requirements for a specific surgical procedure, the robot-assisted beating-heart surgical system can be designed. The controllers for the system should automatically compensate for the beating heart's motion while providing nonoscillatory haptic feedback for the human operator.

References

- Abayazid, M., Kemp, M., Misra, S., 2013. 3D flexible needle steering in soft-tissue phantoms using fiber Bragg grating sensors. In: IEEE International Conference on Robotics and Automation (ICRA), IEEE, pp. 5843–5849.
- Abolhassani, N., Patel, R.V., Ayazi, F., 2007. Minimization of needle deflection in robot-assisted percutaneous therapy. *Int. J. Med. Robot. Comput. Assist. Surg.* 3 (2), 140–148.
- Angelini, G.D., Taylor, F.C., Reeves, B.C., Ascione, R., 2002. Early and midterm outcome after off-pump and on-pump surgery in beating heart against cardioplegic arrest studies (BHACAS 1 and 2): a pooled analysis of two randomised controlled trials. *Lancet* 359 (9313), 1194–1199.
- Asadian, A., Patel, R.V., Kermani, M.R., 2011. A distributed model for needle-tissue friction in percutaneous interventions. In: 2011 IEEE International Conference on Robotics and Automation (ICRA), IEEE, pp. 1896–1901.
- Bachta, W., Renaud, P., Cuvillon, L., Laroche, E., Forgione, A., Gangloff, J., 2009. Motion prediction for computer-assisted beating heart surgery. *IEEE Trans. Biomed. Eng.* 56 (11), 2551–2563.
- Bachta, W., Renaud, P., Laroche, E., Gangloff, J., 2009. Cardiolock2: parallel singularities for the design of an active heart stabilizer. ICRA, pp. 3839–3844.
- Bachta, W., Renaud, P., Laroche, E., Forgione, A., Gangloff, J., 2011. Active stabilization for robotized beating heart surgery. *IEEE Trans. Robot.* 27 (4), 757–768.
- Bebek, O., Cavusoglu, M.C., 2007. Intelligent control algorithms for robotic-assisted beating heart surgery. *IEEE Trans. Robot.* 23 (3), 468–480.
- Bellinger, D.C., Wypij, D., Kuban, K.C.K., Rappaport, L.A., Hickey, P.R., Wernovsky, G., Jonas, R.A., Newburger, J.W., 1999. Developmental and neurological status of children at 4 years of age after heart surgery with hypothermic circulatory arrest or low-flow cardiopulmonary bypass. *Circulation* 100 (5), 526–532.
- Bernardes, M.C., Adorno, B.V., Poignet, P., Zemiti, N., Borges, G.A., 2011. Adaptive path planning for steerable needles using duty-cycling. In: 2011 IEEE/RSJ International Conference on Intelligent Robots and Systems (IROS), IEEE, pp. 2545–2550.
- Bernardes, M.C., Adorno, B.V., Poignet, P., Borges, G.A., 2013. Robot-assisted automatic insertion of steerable needles with closed-loop imaging feedback and intraoperative trajectory replanning. *Mechatronics* 23 (6), 630–645.
- Bernardes, M.C., Adorno, B.V., Borges, G.A., Poignet, P., 2014. 3D robust online motion planning for steerable needles in dynamic workspaces using duty-cycled rotation. *J. Control Autom. Electr. Syst.* 25 (2), 216–227.
- Bobrenkov, O.A., Lee, J., Park, W., 2014. A new geometry-based plan for inserting flexible needles to reach multiple targets. *Robotica* 32 (6), 985–1004.

- Bowthorpe, M., Tavakoli, M., 2016. Generalized predictive control of a surgical robot for beating-heart surgery under delayed and slowly-sampled ultrasound image data. *IEEE Robot. Autom. Lett.* 1 (2), 892–899.
- Bowthorpe, M., Tavakoli, M., 2016. Physiological organ motion prediction and compensation based on multirate, delayed, and unregistered measurements in robot-assisted surgery and therapy. *IEEE/ASME Trans. Mechatron.* 21 (2), 900–911.
- Bowthorpe, M., Tavakoli, M., 2016. Ultrasound-based image guidance and motion compensating control for robot-assisted beating-heart surgery. *J. Med. Robot. Res.* 1 (1), 1640002.
- Bowthorpe, M., Castonguay-Siu, V., Tavakoli, M., 2014. Development of a robotic system to enable beating-heart surgery. *J. Robot. Soc. Jpn* 32 (4), 339–346.
- Bowthorpe, M., Tavakoli, M., Becher, H., Howe, R., 2014. Smith predictor-based robot control for ultrasound-guided teleoperated beating-heart surgery. *IEEE J. Biomed. Health Inform.* 18 (1), 157–166.
- Cheng, L., Tavakoli, M., 2018. Switched-impedance control of surgical robots in teleoperated beating-heart surgery. *J. Med. Robot. Res.* 3, 1841003.
- Cheng, L., Tavakoli, M., 2018. Ultrasound image guidance and robot impedance control for beating-heart surgery. *Control. Eng. Pract.* 81, 9–17.
- Cheng, L., Sharifi, M., Tavakoli, M., 2018. Towards robot-assisted anchor deployment in beating-heart mitral valve surgery. *Int. J. Med. Robot. Comput. Assist. Surg.* 14 (3), e1900.
- Chentanez, N., Alterovitz, R., Ritchie, D., Cho, L., Hauser, K.K., Goldberg, K., Shewchuk, J.R., O'Brien, J.F., 2009. Interactive simulation of surgical needle insertion and steering. *ACM Trans. Graph.* 28(3). <https://doi.org/10.1145/1531326.1531394>.
- Cortesao, R., Dominici, M., 2017. Robot force control on a beating heart. *IEEE/ASME Trans. Mechatron.* 22 (4), 1736–1743.
- Craig, J.J., 2005. *Introduction to Robotics: Mechanics and Control.* vol. 3 Pearson Prentice Hall, Upper Saddle River, NJ.
- Dacey, L.J., Likosky, D.S., Leavitt, B.J., Lahey, S.J., Quinn, R.D., Hernandez Jr., F., Quinton, H.B., Desimone, J.P., Ross, C.S., O'Connor, G.T., et al., 2005. Perioperative stroke and long-term survival after coronary bypass graft surgery. *Ann. Thorac. Surg.* 79 (2), 532–536.
- Dehghan, E., Salcudean, S.E., 2009. Needle insertion parameter optimization for brachytherapy. *IEEE Trans. Robot.* 25 (2), 303–315.
- DiMaio, S.P., Salcudean, S.E., 2003. Needle insertion modeling and simulation. *IEEE Trans. Robot. Autom.* 19 (5), 864–875.
- DiMaio, S.P., Salcudean, S.E., 2005. Interactive simulation of needle insertion models. *IEEE Trans. Biomed. Eng.* 52 (7), 1167–1179.
- Dodds, S.J., et al., 2015. *Feedback Control.* Springer, London, p. 5.
- Dominici, M., Cortesao, R., 2014. Cascade robot force control architecture for autonomous beating heart motion compensation with model predictive control and active observer. In: 2014 5th IEEE RAS & EMBS International Conference on Biomedical Robotics and Biomechatronics, IEEE, pp. 745–751.
- Dominici, M., Cortesao, R., 2014. Model predictive control architectures with force feedback for robotic-assisted beating heart surgery. In: 2014 IEEE International Conference on Robotics and Automation (ICRA), IEEE, pp. 2276–2282.
- Duan, Y., Patil, S., Schulman, J., Goldberg, K., Abbeel, P., 2014. Planning locally optimal, curvature-constrained trajectories in 3D using sequential convex optimization. In: 2014 IEEE International Conference on Robotics and Automation (ICRA), IEEE, pp. 5889–5895.
- Duindam, V., Alterovitz, R., Sastry, S., Goldberg, K., 2008. Screw-based motion planning for bevel-tip flexible needles in 3D environments with obstacles. In: IEEE International Conference on Robotics and Automation, 2008. ICRA 2008, IEEE, pp. 2483–2488.

- Duindam, V., Xu, J., Alterovitz, R., Sastry, S., Goldberg, K., 2010. Three-dimensional motion planning algorithms for steerable needles using inverse kinematics. *Int. J. Robot. Res.* 29 (7), 789–800.
- Fallah, B., Khadem, M., Rossa, C., Sloboda, R., Usmani, N., Tavakoli, M., 2015. Extended bicycle model for needle steering in soft tissue. 2015 IEEE/RSJ International Conference on Intelligent Robots and Systems (IROS), IEEE, pp. 4375–4380.
- Fallah, B., Rossa, C., Sloboda, R., Usmani, N., Tavakoli, M., 2016. Partial estimation of needle tip orientation in generalized coordinates in ultrasound image-guided needle insertion. In: IEEE International Conference on Advanced Intelligent Mechatronics (AIM), 2016, IEEE, pp. 1604–1609.
- Fallah, B., Rossa, C., Sloboda, R.S., Usmani, N., Tavakoli, M., 2016. Sliding-based switching control for image-guided needle steering in soft tissue. *IEEE Robot. Autom. Lett.* 1 (2), 860–867.
- Fallah, B., Rossa, C., Sloboda, R.S., Usmani, N., Tavakoli, M., 2017. Sliding-based image-guided 3D needle steering in soft tissue. *Control. Eng. Pract.* 63, 34–43.
- Fallah, B., Sloboda, R., Usmani, N., Tavakoli, M., 2018. Model averaging and input transformation for 3D needle steering. *J. Med. Robot. Res.* 3, 1841004.
- Fix, J., Isada, L., Cosgrove, D., Miller, D.P., Savage, R., Blum, J., Stewart, W., 1993. Do patients with less than “echo-perfect” results from mitral valve repair by intraoperative echocardiography have a different outcome? *Circulation* 88 (5 Pt. 2), II39–II48.
- Gangloff, J., Ginhoux, R., de Mathelin, M., Soler, L., Marescaux, J., 2006. Model predictive control for compensation of cyclic organ motions in teleoperated laparoscopic surgery. *IEEE Trans. Control Syst. Technol.* 14 (2), 235–246.
- Ginhoux, R., Gangloff, J.A., De Mathelin, M.F., Soler, L., Sanchez, M.M.A., Marescaux, J., 2004. Beating heart tracking in robotic surgery using 500 Hz visual servoing, model predictive control and an adaptive observer. In: 2004 IEEE International Conference on Robotics and Automation, 2004. Proceedings. ICRA'04, vol. 1. IEEE, pp. 274–279.
- Ginhoux, R., Gangloff, J., de Mathelin, M., Soler, L., Sanchez, M.M.A., Marescaux, J., et al., 2005. Active filtering of physiological motion in robotized surgery using predictive control. *IEEE Trans. Robot.* 21 (1), 67–79.
- Glozman, D., Shoham, M., 2004. Flexible needle steering and optimal trajectory planning for percutaneous therapies. International Conference on Medical Image Computing and Computer-Assisted Intervention, Springer, pp. 137–144.
- Goksel, O., Salcudean, S.E., Dimaio, S.P., 2006. 3D simulation of needle-tissue interaction with application to prostate brachytherapy. *Comput. Aided Surg.* 11 (6), 279–288.
- Guthart, G.S., Salisbury, J.K., 2000. The intuitive™ telesurgery system: overview and applications. *IEEE International Conference on Robotics and Automation*, 2000. Proceedings. ICRA'00, vol. 1. IEEE, pp. 618–621.
- Haddadi, A., Goksel, O., Salcudean, S.E., Hashtrudi-Zaad, K., 2010. On the controllability of dynamic model-based needle insertion in soft tissue. In: 2010 Annual International Conference of the IEEE Engineering in Medicine and Biology Society (EMBC), IEEE, pp. 2287–2291.
- Hogan, N., 1984. Impedance control: an approach to manipulation. American Control Conference, 1984, IEEE, pp. 304–313.
- Hogan, N., 1985. Impedance control: an approach to manipulation: part II—implementation. *J. Dyn. Syst. Meas. Control* 107 (1), 8–16.
- Kallem, V., Cowan, N.J., 2009. Image guidance of flexible tip-steerable needles. *IEEE Trans. Robot.* 25 (1), 191–196.
- Kallem, V., Chang, D.E., Cowan, N.J., 2011. Observer design for needle steering using task-induced symmetry and reduction. *IFAC Proc. Vol.* 44 (1), 8028–8033.
- Kaya, M., Bebek, O., 2014. Needle localization using Gabor filtering in 2D ultrasound images. In: 2014 IEEE International Conference on Robotics and Automation (ICRA), IEEE, pp. 4881–4886.

- Kesner, S.B., Howe, R.D., 2011. Force control of flexible catheter robots for beating heart surgery. *IEEE International Conference on Robotics and Automation. ICRA, NIH Public Access*, p. 1589.
- Kesner, S.B., Howe, R.D., 2011. Position control of motion compensation cardiac catheters. *IEEE Trans. Robot.* 27 (6), 1045–1055.
- Kesner, S.B., Howe, R.D., 2014. Robotic catheter cardiac ablation combining ultrasound guidance and force control. *Int. J. Robot. Res.* 33 (4), 631–644.
- Kettler, D.T., Plowes, R.D., Novotny, P.M., Vasilyev, N.V., Pedro, J., Howe, R.D., 2007. An active motion compensation instrument for beating heart mitral valve surgery. In: *IEEE/RSJ International Conference on Intelligent Robots and Systems, 2007. IROS 2007*, IEEE, pp. 1290–1295.
- Khadem, M., Rossa, C., Sloboda, R.S., Usmani, N., Tavakoli, M., 2016. Ultrasound-guided model predictive control of needle steering in biological tissue. *J. Med. Robot. Res.* 1 (1), 1640007.
- Khoshnam, M., Patel, R.V., 2017. Robotics-assisted control of steerable ablation catheters based on the analysis of tendon-sheath transmission mechanisms. *IEEE/ASME Trans. Mechatron.* 22 (3), 1473–1484.
- Liu, X., Tavakoli, M., 2011. Adaptive inverse dynamics four-channel control of uncertain nonlinear teleoperation systems. *Adv. Robot.* 25 (13–14), 1729–1750.
- Majewicz, A., Siegel, J.J., Stanley, A.A., Okamura, A.M., 2014. Design and evaluation of duty-cycling steering algorithms for robotically-driven steerable needles. In: *IEEE International Conference on Robotics and Automation (ICRA)*, IEEE, pp. 5883–5888.
- Malekian, L., Talebi, H.A., Towhidkhah, F., 2013. Needle detection in 3D ultrasound images using anisotropic diffusion and robust fitting. *International Symposium on Artificial Intelligence and Signal Processing*, Springer, pp. 111–120.
- Mansouri, S., Farahmand, F., Vossoughi, G., Ghavidel, A.A., 2018. A hybrid algorithm for prediction of varying heart rate motion in computer-assisted beating heart surgery. *J. Med. Syst.* 42 (10), 200.
- Minhas, D.S., Engh, J.A., Fenske, M.M., Riviere, C.N., 2007. Modeling of needle steering via duty-cycled spinning. In: *29th Annual International Conference of the IEEE Engineering in Medicine and Biology Society, 2007. EMBS 2007*, IEEE, pp. 2756–2759.
- Misra, S., Reed, K.B., Schafer, B.W., Ramesh, K.T., Okamura, A.M., 2010. Mechanics of flexible needles robotically steered through soft tissue. *Int. J. Robot. Res.* 29 (13), 1640–1660.
- Moharerri, O., Schneider, C., Salcudean, S., 2014. Bimanual telerobotic surgery with asymmetric force feedback: a DaVinci® surgical system implementation. In: *2014 IEEE/RSJ International Conference on Intelligent Robots and Systems (IROS 2014)*, IEEE, pp. 4272–4277.
- Moreira, P., Liu, C., Zemiti, N., Poignet, P., 2012. Beating heart motion compensation using active observers and disturbance estimation. *IFAC Proc. Vol.* 45 (22), 741–746.
- Moreira, P., Patil, S., Alterovitz, R., Misra, S., 2014. Needle steering in biological tissue using ultrasound-based online curvature estimation. In: *IEEE International Conference on Robotics and Automation (ICRA)*, 2014, IEEE, pp. 4368–4373.
- Moreira, P., Zemiti, N., Liu, C., Poignet, P., 2014. Viscoelastic model based force control for soft tissue interaction and its application in physiological motion compensation. *Comput. Methods Prog. Biomed.* 116 (2), 52–67.
- Motaharifar, M., Talebi, H.A., Abdollahi, F., Afshar, A., 2015. Nonlinear adaptive output-feedback controller design for guidance of flexible needles. *IEEE/ASME Trans. Mechatron.* 20 (4), 1912–1919.
- Nakajima, Y., Nozaki, T., Ohnishi, K., 2014. Heartbeat synchronization with haptic feedback for telesurgical robot. *IEEE Trans. Ind. Electron.* 61 (7), 3753–3764.
- Nakamura, Y., Kishi, K., Kawakami, H., et al., 2001. Heartbeat synchronization for robotic cardiac surgery. *ICRA*, vol. 2, pp. 2014–2019.

- Newman, M.F., Kirchner, J.L., Phillips-Bute, B., Gaver, V., Grocott, H., Jones, R.H., Mark, D.B., Reves, J.G., Blumenthal, J.A., 2001. Longitudinal assessment of neurocognitive function after coronary-artery bypass surgery. *N. Engl. J. Med.* 344 (6), 395–402.
- Paparella, D., Yau, T.M., Young, E., 2002. Cardiopulmonary bypass induced inflammation: pathophysiology and treatment. An update. *Eur. J. Cardiothorac. Surg.* 21 (2), 232–244.
- Park, W., Wang, Y., Chirikjian, G.S., 2010. The path-of-probability algorithm for steering and feedback control of flexible needles. *Int. J. Robot. Res.* 29 (7), 813–830.
- Patil, S., Alterovitz, R., 2010. Interactive motion planning for steerable needles in 3D environments with obstacles. In: 3rd IEEE RAS and EMBS International Conference on Biomedical Robotics and Biomechatronics (BioRob), 2010, IEEE, pp. 893–899.
- Reed, K.B., Kallem, V., Alterovitz, R., Goldberg, K., Okamura, A.M., Cowan, N.J., 2008. Integrated planning and image-guided control for planar needle steering. In: 2nd IEEE RAS & EMBS International Conference on Biomedical Robotics and Biomechatronics, 2008. BioRob 2008, IEEE, pp. 819–824.
- Richa, R., Poignet, P., Liu, C., 2010. Three-dimensional motion tracking for beating heart surgery using a thin-plate spline deformable model. *Int. J. Robot. Res.* 29 (2–3), 218–230.
- Richa, R., Bó, A.P.L., Poignet, P., 2011. Towards robust 3D visual tracking for motion compensation in beating heart surgery. *Med. Image Anal.* 15 (3), 302–315.
- Rossa, C., Sloboda, R., Usmani, N., Tavakoli, M., 2016. Estimating needle tip deflection in biological tissue from a single transverse ultrasound image: application to brachytherapy. *Int. J. Comput. Assist. Radiol. Surg.* 11 (7), 1347–1359.
- Rucker, D.C., Das, J., Gilbert, H.B., Swaney, P.J., Miga, M.I., Sarkar, N., Webster, R.J., 2013. Sliding mode control of steerable needles. *IEEE Trans. Robot.* 29 (5), 1289–1299.
- Ruszkowski, A., Moharer, O., Lichtenstein, S., Cook, R., Salcudean, S., 2015. On the feasibility of heart motion compensation on the DaVinci® surgical robot for coronary artery bypass surgery: implementation and user studies. 2015 IEEE International Conference on Robotics and Automation (ICRA), IEEE, pp. 4432–4439.
- Ruszkowski, A., Schneider, C., Moharer, O., Salcudean, S., 2016. Bimanual teleoperation with heart motion compensation on the DaVinci® research kit: implementation and preliminary experiments. In: IEEE International Conference on Robotics and Automation (ICRA), 2016, IEEE, pp. 4101–4108.
- Schulman, J., Duan, Y., Ho, J., Lee, A., Awwal, I., Bradlow, H., Pan, J., Patil, S., Goldberg, K., Abbeel, P., 2014. Motion planning with sequential convex optimization and convex collision checking. *Int. J. Robot. Res.* 33 (9), 1251–1270.
- Schweikard, A., Glosser, G., Bodduluri, M., Murphy, M.J., Adler, J.R., 2000. Robotic motion compensation for respiratory movement during radiosurgery. *Comput. Aided Surg.* 5 (4), 263–277.
- Sharifi, M., Salarieh, H., Behzadipour, S., Tavakoli, M., 2018. Beating-heart robotic surgery using bilateral impedance control: theory and experiments. *Biomed. Signal Process. Control* 45, 256–266.
- Shkolnik, A., Walter, M., Tedrake, R., 2009. Reachability-guided sampling for planning under differential constraints. In: IEEE International Conference on Robotics and Automation, 2009. ICRA'09, IEEE, pp. 2859–2865.
- Sovizi, J., Kumar, S., Krovi, V., 2016. Approximating Markov chain approach to optimal feedback control of a flexible needle. *J. Dyn. Syst. Meas. Control* 138 (11), 111006.
- Swensen, J.P., Lin, M., Okamura, A.M., Cowan, N.J., 2014. Torsional dynamics of steerable needles: modeling and fluoroscopic guidance. *IEEE Trans. Biomed. Eng.* 61 (11), 2707–2717.
- Taghirad, H.D., 2013. Parallel Robots: Mechanics and Control. CRC Press, Boca Raton, FL.

- Taschereau, R., Pouliot, J., Roy, J., Tremblay, D., 2000. Seed misplacement and stabilizing needles in transperineal permanent prostate implants. *Radiat. Oncol.* 55 (1), 59–63.
- Tavakoli, M., 2008. Haptics for Teleoperated Surgical Robotic Systems. vol. 1. World Scientific, Singapore.
- Tavakoli, M., Aziminejad, A., Patel, R.V., Moallem, M., 2007. High-fidelity bilateral teleoperation systems and the effect of multimodal haptics. *IEEE Trans. Syst. Man Cybern. B Cybern.* 37 (6), 1512–1528.
- Torre, L.A., Bray, F., Siegel, R.L., Ferlay, J., Lortet-Tieulent, J., Jemal, A., 2015. Global cancer statistics, 2012. *CA Cancer J. Clin.* 65 (2), 87–108.
- Tuna, E.E., Franke, T.J., Bebek, O., Shiose, A., Fukamachi, K., Cavusoglu, M.C., 2013. Heart motion prediction based on adaptive estimation algorithms for robotic-assisted beating heart surgery. *IEEE Trans. Robot.* 29 (1), 261–276.
- Uherčík, M., Liebgott, H., Kybic, J., Cachard, C., 2009. Needle localization methods in 3D ultrasound data. International Congress on Ultrasonics, pp. 11–17.
- Vrooijink, G.J., Abayazid, M., Patil, S., Alterovitz, R., Misra, S., 2014. Needle path planning and steering in a three-dimensional non-static environment using two-dimensional ultrasound images. *Int. J. Robot. Res.* 33 (10), 1361–1374.
- Wagner, C.R., Stylopoulos, N., Jackson, P.G., Howe, R.D., 2007. The benefit of force feedback in surgery: examination of blunt dissection. *Presence Teleop. Virt. Environ.* 16 (3), 252–262.
- Waine, M., Rossa, C., Sloboda, R., Usmani, N., Tavakoli, M., 2016. Three-dimensional needle shape estimation in TRUS-guided prostate brachytherapy using 2-D ultrasound images. *IEEE J. Biomed. Health Inform.* 20 (6), 1621–1631.
- Wallner, K., Ellis, W., Russell, K., Cavanagh, W., Blasko, J., 1999. Use of TRUS to predict pubic arch interference of prostate brachytherapy. *Int. J. Radiat. Oncol. Biol. Phys.* 43 (3), 583–585.
- Wang, J., Li, X., Zheng, J., Sun, D., 2014. Dynamic path planning for inserting a steerable needle into a soft tissue. *IEEE/ASME Trans. Mechatron.* 19 (2), 549–558.
- Webster, R.J., Kim, J.S., Cowan, N.J., Chirikjian, G.S., Okamura, A.M., 2006. Non-holonomic modeling of needle steering. *Int. J. Robot. Res.* 25 (5–6), 509–525.
- Yan, K., Ng, W.S., Ling, K.V., Yu, Y., Podder, T., Liu, T.-I., Cheng, C.W.S., 2006. Needle steering modeling and analysis using unconstrained modal analysis. In: The First IEEE/RAS-EMBS International Conference on Biomedical Robotics and Biomechatronics, BioRob 2006, IEEE, pp. 87–92.
- Yan, K.G., Podder, T., Yu, Y., Liu, T.-I., Cheng, C.W.S., Ng, W.S., 2009. Flexible needle-tissue interaction modeling with depth-varying mean parameter: preliminary study. *IEEE Trans. Biomed. Eng.* 56 (2), 255–262.
- Yang, B., Liu, C., Poignet, P., Zheng, W., Liu, S., 2015. Motion prediction using dual Kalman filter for robust beating heart tracking. 37th Annual International Conference of the IEEE Engineering in Medicine and Biology Society (EMBC), IEEE, pp. 4875–4878.
- Yuen, S., Kesner, S., Vasilyev, N., Del Nido, P., Howe, R., 2008. 3D ultrasound-guided motion compensation system for beating heart mitral valve repair. Medical Image Computing and Computer-Assisted Intervention—MICCAI 2008, 711–719.
- Yuen, S.G., Kettler, D.T., Novotny, P.M., Plowes, R.D., Howe, R.D., 2009. Robotic motion compensation for beating heart intracardiac surgery. *Int. J. Robot. Res.* 28 (10), 1355–1372.
- Yuen, S.G., Perrin, D.P., Vasilyev, N.V., Pedro, J., Howe, R.D., 2010. Force tracking with feed-forward motion estimation for beating heart surgery. *IEEE Trans. Robot.* 26 (5), 888–896.
- Zahraee, A.H., Paik, J.K., Szewczyk, J., Morel, G., 2010. Toward the development of a hand-held surgical robot for laparoscopy. *IEEE ASME Trans. Mechatron.* 15 (6), 853.

- Zarrouk, Z., Chemori, A., Poignet, P., 2010. Adaptive force feedback control for 3D compensation of physiological motion in beating heart surgery. In: IEEE/RSJ International Conference on Intelligent Robots and Systems (IROS), IEEE, pp. 1856–1861.
- Zeithofer, J., Asenbaum, S., Spiss, C., Wimmer, A., Mayr, N., Wolnar, E., Deecke, L., 1993. Central nervous system function after cardiopulmonary bypass. *Eur. Heart J.* 14 (7), 885–890.
- Zhao, Y., Liebgott, H., Cachard, C., 2012. Tracking micro tool in a dynamic 3D ultrasound situation using Kalman filter and RANSAC algorithm. In: 9th IEEE International Symposium on Biomedical Imaging (ISBI), IEEE, pp. 1076–1079.
- Zhao, Y., Cachard, C., Liebgott, H., 2013. Automatic needle detection and tracking in 3D ultrasound using an ROI-based RANSAC and Kalman method. *Ultrason. Imaging* 35 (4), 283–306.